JGR Space Physics

RESEARCH ARTICLE
10.1029/2023JA031913

A Model of Hourly Variations of the Near-Earth Magnetic Field Generated in the Inner Magnetosphere and Its Induced Counterpart

M. Fillion[1,2], A. Chulliat[1,2], P. Alken[1,2], M. Kruglyakov[3], and A. Kuvshinov[4,5]

[1]Cooperative Institute for Research in Environmental Sciences, University of Colorado, Boulder, CO, USA, [2]NOAA National Centers for Environmental Information, Boulder, CO, USA, [3]Department of Physics, University of Otago, Otago, New Zealand, [4]Institute of Geophysics, ETH Zürich, Zürich, Switzerland, [5]Institute of Solar-Terrestrial Physics, Siberian Branch of Russian Academy of Sciences, Irkutsk, Russia

Key Points:

- A new ground-data based model of hourly variations of the primary inner near-Earth magnetospheric and associated induced field is presented
- Comparison with satellite data shows up to 20% performance improvement compared to the CHAOS-7 model for moderate and active times
- The model accounts for variations of the field with local time and can be used to study geomagnetic storms

Supporting Information:

Supporting Information may be found in the online version of this article.

Correspondence to:

M. Fillion,
martin.fillion@colorado.edu

Citation:

Fillion, M., Chulliat, A., Alken, P., Kruglyakov, M., & Kuvshinov, A. (2023). A model of hourly variations of the near-Earth magnetic field generated in the inner magnetosphere and its induced counterpart. *Journal of Geophysical Research: Space Physics*, *128*, e2023JA031913. https://doi.org/10.1029/2023JA031913

Received 31 JUL 2023
Accepted 9 NOV 2023

Author Contributions:

Conceptualization: M. Fillion, A. Chulliat, P. Alken, M. Kruglyakov, A. Kuvshinov
Formal analysis: M. Fillion, A. Chulliat, P. Alken
Funding acquisition: A. Chulliat, P. Alken
Investigation: M. Fillion, A. Chulliat, P. Alken
Methodology: M. Fillion, A. Chulliat, P. Alken, M. Kruglyakov, A. Kuvshinov
Project Administration: A. Chulliat, P. Alken
Resources: A. Chulliat, P. Alken
Software: M. Fillion, M. Kruglyakov, A. Kuvshinov
Supervision: A. Chulliat, P. Alken
Validation: M. Fillion, A. Chulliat, P. Alken

Abstract

We present a new model of the near-Earth magnetospheric field produced by electric currents in the inner magnetosphere and the associated induced magnetic field. The model is designed to track hourly variations of these fields and accounts for their local time asymmetries. It is built by applying spherical harmonic analysis to vector measurements from the ground observatory network at low and mid-latitudes. The primary and induced fields are separated with an approach in the time domain that uses a *a priori* radially-symmetric electric conductivity model of the Earth. The model coefficients are computed at one-hour time steps between 1997 and 2022. This model is shown to be consistent to within a few nT with previously developed indices which track the magnetospheric ring current. It is also validated against data from the Swarm, CHAMP and Ørsted satellites. The fit to satellite data is comparable to that of the CHAOS-7.15 model for geomagnetically quiet times, and improved by up to 20% on some components for geomagnetically moderate and active times. We attribute these differences mostly to a better representation of local time asymmetries, both on average and during individual geomagnetic storms. This model can be used in various applications, such as investigating the properties of the magnetospheric field and its sources and separating the magnetospheric field from the fields of other sources in geomagnetic field modeling.

Plain Language Summary

Geomagnetic field modeling aims at building data-based mathematical representations, or models, of the various contributions to the total Earth's magnetic field measured at or near the Earth's surface. One of such contributions is the magnetic field generated by electric currents in the inner magnetosphere, including the so-called ring current. In this paper, we present a new model of the near-Earth magnetic field generated in the inner magnetosphere based on data collected in ground magnetic observatories. The model covers the 1997–2022 time span, includes improved representations of the local time asymmetries of the field and of the effect of electrical induction in the Earth's mantle, and is validated against data collected in low Earth orbits by the Swarm, CHAMP and Oersted satellites. We find that the model provides an improved representation of the magnetic field generated in the inner magnetosphere during periods of moderate and high geomagnetic activity, including magnetic storms.

1. Introduction

The geomagnetic field is the sum of the fields produced by electric currents and magnetized rocks in and around the Earth. These sources range from the Earth's outer core to the magnetopause, beyond which the interplanetary magnetic field carried by the solar wind dominates. In the near-Earth environment, typically up to a few thousand km altitude, the geomagnetic field is referred to as the near-Earth geomagnetic field (Langel et al., 1996; Sabaka et al., 2002). In this region, the most important components of the geomagnetic field are the core (or main) field, produced by liquid iron flows within the outer core, the lithospheric field, generated by magnetized rocks in the lithosphere, the ionospheric field, produced by electric currents in the ionosphere, and the magnetospheric field, produced by electric currents in the magnetosphere (Hulot et al., 2015). Additionally, the time-varying external fields induce currents in the electrically conducting mantle, which in turn produce secondary magnetic fields. All these fields vary on a large range of spatial and temporal scales (Olsen & Stolle, 2012).

Improving data-based models of the near-Earth magnetospheric field has become an important topic in geomagnetism as these models are used in a variety of applications. Building such models, however, relies on separating

Visualization: M. Fillion
Writing – original draft: M. Fillion
Writing – review & editing: M. Fillion, A. Chulliat, P. Alken, M. Kruglyakov, A. Kuvshinov

the near-Earth magnetospheric field from the fields of other sources in magnetic data, which remains a challenging task due to the significant overlap of spatial and temporal scales, and the insufficient spatio-temporal coverage of magnetic field data collected by ground-based observatories and low-Earth orbit (LEO) satellites. For example, due to the overlap of its spatial scales with those of the core field on the night side of the Earth, accurately removing the magnetospheric field is an essential step in building modern core field models used to constrain physical processes in the Earth's core and the geodynamo (Finlay et al., 2017). Magnetospheric field models are also used in ionospheric magnetic field and electrodynamics studies (Fillion et al., 2023; Stolle et al., 2016). Additionally, in a certain frequency range, the near-Earth magnetospheric field is one of the main sources for the electromagnetic induction studies of the Earth's interior (A. Kuvshinov et al., 2021) as well as a signature of the interactions between the solar wind and the magnetosphere (Milan et al., 2017). Improved modeling of the near-Earth magnetospheric field would thus provide opportunities to better model other geomagnetic field sources, better constrain the conductivity structure of the Earth, and better characterize the magnetospheric electric current system.

The primary large-scale current systems contributing to the near-Earth magnetospheric field are well identified. Those are the symmetric and partial ring currents, the magnetopause and the magnetotail currents. It is customary to distinguish between electric currents in the inner magnetosphere and the outer magnetosphere. In the inner magnetosphere, the motion of electrons and ions is primarily determined by the geometry of the dominant dipole component of the main field, whereas, in the outer magnetosphere, the main field is weaker, and the geometry of electric currents is controlled by interactions between the main field and the solar wind (Lühr et al., 2017; Maus & Lühr, 2005). For modeling purpose, it is conceptually useful to assume that the symmetric and partial ring currents are confined to the inner magnetosphere, whereas the magnetopause and magnetotail currents flow in the outer magnetosphere. The reader should be aware that this representation, however, does not reflect the full complexity of magnetospheric electric currents. For instance, the inner edge of the magnetotail currents can move earthward inside the inner magnetosphere during geomagnetic storms (Alexeev et al., 1996). Various field-aligned currents additionally connect magnetospheric currents to ionospheric currents, mostly at high latitudes. A detailed review of the morphology and dynamics of these currents can be found in Ganushkina et al. (2018).

There is a long tradition of attempting to characterize geomagnetic activity using simplified indices. Some indices were designed to describe the intensity of the field produced by electric currents in the inner magnetosphere, and in particular the field of the symmetric part of the ring current at the Earth's surface. In practice, however, these indices may contain magnetic field signals from electric currents other than the ring current and some authors have challenged the use of such indices during geomagnetic storms (Sandhu et al., 2021; Turner et al., 2000). Among these, the Dst index (Sugiura, 1963), the RC index (Olsen et al., 2014), the SYM-H index (Iyemori et al., 2010), the SMR index (Newell & Gjerloev, 2012), and the VMD index (Thomson & Lesur, 2007) are derived using ground magnetic data and have a time resolution ranging from 1 minute to 1 hour. Equivalent indices have also been derived using LEO satellite data (Balasis et al., 2019; Burke et al., 2011; Papadimitriou et al., 2021). Additionally, some other ground-based indices attempt to characterize the local-time asymmetry of the inner magnetospheric field, such as the ASY (Iyemori et al., 2010) and SMR-LT (Newell & Gjerloev, 2012) indices. No equivalent index, however, was developed to describe the intensity of the field produced by electric currents in the outer magnetosphere, although a proxy was proposed by Lühr et al. (2017). This proxy can be computed using predictions of the polar cap boundary by an empirical model of the auroral oval (Xiong & Lühr, 2014).

Ground-based indices have often been used in data-based, spherical harmonic models of the near-Earth geomagnetic field to track the fast variations—in this paper, fast variations refer to time variations of the order of 1 hour to tens of minutes—of the low degree primary magnetospheric fields produced by electric currents in the inner magnetosphere and their induced counterparts. Such models generally aim to represent the field during quiet geomagnetic times. This was the case, for example, with the early models of the Comprehensive Model series, in which the amplitude of the ring current magnetic field was proportional to the Dst index (Sabaka & Olsen, 2006; Sabaka et al., 2002, 2004). Later versions adopted a different approach where the degree 1 primary and induced magnetospheric fields were assumed static in one-hour bins and inferred from the data (Sabaka et al., 2015, 2018, 2020). Similarly, the GRIMM (Lesur et al., 2008, 2010, 2015), POMME (Maus et al., 2005, 2006) and CHAOS (Finlay et al., 2016, 2020; Olsen et al., 2014) models relied on the VMD, Dst and RC indices, respectively, to capture fast magnetospheric field variations of the order of 1 hour to 20 min.

Additionally, a model of the rapid near-Earth magnetospheric field was also developed in the context of the Swarm satellite mission (Hamilton, 2013). In some of these models, the near-Earth magnetospheric field is sometimes decomposed into its Solar Magnetic (SM) and Geocentric Solar Magnetospheric (GSM) components–a definition of these two coordinates system can be found in Laundal and Richmond (2017). The SM coordinates are well adapted to represent the field from inner magnetospheric currents, whereas the GSM coordinates are well suited to represent the field produced by outer magnetospheric currents (Maus & Lühr, 2005; Olsen et al., 2005). It is also worth mentioning that some parallel efforts have focused on modeling the distant magnetospheric field, that is, from several Earth's radii up to the magnetopause. In this region, as opposed to the near-Earth environment, the ionospheric field can be neglected (Tsyganenko et al., 2021). Some examples of such models include the Tsyganenko model series as well as other models, which are reviewed in detail in Tsyganenko et al. (2021).

The treatment of the induced near-Earth magnetospheric field in data-based geomagnetic field models has received special attention over the years as this field represents between 30% and 40% of the total magnetospheric field. In principle, one could separate the induced and primary fields using the Gauss method (Olsen et al., 2010). Recent models, however, have favored another approach based on transfer functions in the frequency domain particularly suited for use in conjunction with spherical harmonics (Püthe & Kuvshinov, 2014; A. Kuvshinov et al., 2021). This approach can be applied to both ground and satellite data, but requires the a priori knowledge of the electric conductivity structure of the Earth. Despite its proven effectiveness, it is nevertheless difficult to use in real time. Besides, the approach could suffer from potential spatio-temporal aliasing when applied to satellite data. These limitations triggered the development of time-domain approaches, that were first applied to separate the Dst index into internal and external parts (Maus & Weidelt, 2004; Olsen et al., 2005). More recently, time-domain approaches were used in low-degree spherical harmonic models of hourly variations of the primary (external) and induced (internal) fields (Grayver et al., 2021; Kruglyakov et al., 2022). As applied to ground-based data, these approaches generally do not distinguish between ionospheric and magnetospheric fields, both considered together as one external field.

In recent data-based models, the representation of fast variations of the near-Earth magnetospheric field produced by inner magnetospheric currents is generally limited to a degree and order one spherical harmonic expansion in an Earth-centered coordinate system. Some models include higher degree spherical harmonics to represent slower variations, for example, the average diurnal and seasonal variations. On timescales of 1 hour or less, the near-Earth magnetospheric field is known to have a more complicated morphology. During active geomagnetic times especially, the magnetospheric field can have significant variations in local time, also referred to as local time asymmetries. These asymmetries have been well documented using ground (Akasofu & Chapman, 1964; Love & Gannon, 2009, 2010; Newell & Gjerloev, 2012) and satellite (Le et al., 2011; Lühr & Zhou, 2020b; Stolle et al., 2021) magnetic field data. At low latitudes, they can be particularly observed in the north-south direction. The occurrence of local-time asymmetry during quiet geomagnetic times remains an open question, as is its potential impact on the quality of core field models derived from quiet-time geomagnetic data. A better description of the local time asymmetry might also provide useful constraints on magnetospheric currents themselves. Although some indices, such as SMR-LT, attempt to capture the asymmetric part of the magnetospheric field, to the authors' knowledge, there is no widely available spherical harmonic model of the near-Earth ring current magnetic field to degrees and orders higher than one. Building such a model for fast variations is challenging due to the geographically sparse data coverage and the potential signal leakage from the ionospheric field.

In this study, we build a data-based, low-degree spherical harmonic model of hourly variations of the near-Earth magnetospheric field produced by electric currents in the inner magnetosphere and of the associated induced field generated by the electric currents in the Earth's mantle. We make use of a new time-domain approach to separate the primary and induced fields. The data processing and methodology are presented in Sections 2 and 3. In Section 4, the degree 1 and order 0 coefficients of the new model are compared with the RC index. The performance of the full model is assessed by comparing the model predictions to LEO satellite data in Section 5. In Section 6, we discuss the ability of the model to predict the local time asymmetry of the near-Earth magnetospheric field for various geomagnetic activity conditions and compare our results with those of earlier studies. Section 7 concludes the paper.

2. Data Preprocessing

We use 25 years of quality-controlled, baseline-corrected magnetic observatory hourly mean values spanning 1997–2022 prepared by the British Geological Survey (Macmillan & Olsen, 2013). This data set is distributed

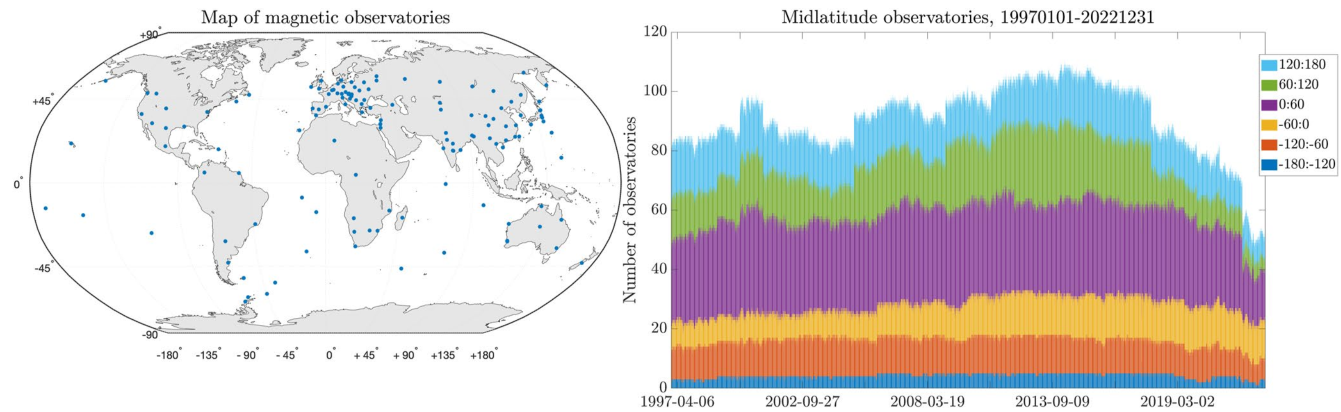

Figure 1. (left) Map of all ground magnetic observatories used in this study. (right) Number of observatories with available data at each one-hour timestep between 1997 and 2022. The color code provides the number of available observatories in each of the six longitude sectors.

as an auxiliary product of the Swarm satellite mission (Olsen et al., 2013). To avoid contamination from the high-latitude ionospheric field and the field produced by the equatorial electrojet, we exclude observatories poleward of 55° and equatorward of 5° quasi dipole latitudes (Richmond, 1995) in both hemispheres. This results in a total number of 135 observatories with varying data availability over the period of time considered in this study. The left panel of Figure 1 shows a map of all 135 magnetic observatories. The spatial coverage is heterogeneous, with good coverage over some continental areas and poor coverage everywhere else, particularly over the Pacific Ocean (There is no observatory at high latitudes due to the applied data selection). The right panel of Figure 1 shows the number of observatories providing data for each one-hour time step and six longitude sectors. Before 2019, the number of observatories varies between 80 and 110, which represents at least 60% of the total number of observatories. After 2019, however, the number of available observatories drops to about 60 due to the decreased availability of recent baseline-corrected observatory data.

To isolate the magnetic field generated in the inner magnetosphere, observatory data are corrected for magnetic fields generated by other sources using various models. The main and crustal fields are removed using the CHAOS-7.15 extension of the CHAOS-7 model (Finlay et al., 2020) and the observatory crustal biases computed by Califf et al. (2022), respectively. These crustal biases were computed using the CHAOS-7 model up to degree 15. Therefore, for consistency, the main field from the CHAOS-7.15 model is also computed up to degree 15 in this study. External fields originating in regions other than the inner magnetosphere are subtracted using two models. First, we use DIFI-7, the most recent version of the DIFI model (Chulliat et al., 2013, 2016), to remove Sq magnetic fields generated by electric currents in the E-region of the ionosphere and induced currents in the Earth's mantle. Second, we use the external part of CHAOS-7.15 in GSM coordinates to remove magnetic fields generated by outer magnetospheric sources, for example, magnetotail and magnetopause currents, and their induced counterpart (cf. Equation 2d in Finlay et al. (2020)). Both DIFI and the outer magnetospheric portion of CHAOS-7.15 are climatological models, that is, they only represent average quiet-time variations of the modeled sources. Therefore, some signals from fast-varying ionospheric and outer magnetospheric fields remain in the data and could possibly leak into the model, especially during periods of high geomagnetic activity.

3. Methodology

We derive hourly time series of low-degree spherical harmonic coefficients of the external magnetospheric field and its induced counterpart in Centered Dipole (CD) coordinates (Laundal & Richmond, 2017) using the preprocessed data. These coefficients are computed using the horizontal component only. This is done to minimize contamination of the model by locally induced magnetic fields, which are generally largest on the vertical component (A. V. Kuvshinov, 2008). The algorithm to derive the coefficients uses a radially-symmetric (1D) a priori electric conductivity model taken from (A. Kuvshinov et al., 2021) (cf. their Table 1). The first (surface) layer of 1D model has a 1 km thickness and represents the globally averaged conductance (9287 S) of landmasses, oceans, and marine sediments. We also stress that the model is only valid at low and mid latitudes, since high latitude data were excluded (cf. Section 2). The algorithm is described in Sections 3.1 and 3.2. Additional details on the treatment of the induced field can be found in Kruglyakov et al. (2022) and Grayver et al. (2021).

3.1. Spherical Harmonics Representation

The ground magnetic observatories measure the magnetic field in a region of space where it can be assumed that no source of the magnetic field exists. In such a region, the magnetic field is said to be potential and can be decomposed in two terms (Sabaka et al., 2010) such as:

$$\vec{B} = \vec{B}_{ext} + \vec{B}_{int} = -\nabla(V_{int} + V_{ext}), \tag{1}$$

where $\vec{B}$ is the total magnetic field measured by a magnetic observatory and expressed in nT, $\vec{B}_{ext}$ is the external magnetic field produced by sources located above the observatory region, $\vec{B}_{int}$ is the internal magnetic field produced by sources located below the observatory region, and $\vec{B}_{ext}$ and $\vec{B}_{int}$ derive from the potentials V_{int} and V_{ext}, respectively. In—and in all the following equations—each term implicitly depends on the radius r, the CD colatitude θ, the CD longitude ϕ and the time t. Similarly, the horizontal component of the magnetic field $\vec{B}$ may be written as:

$$\vec{B}_H = -\frac{1}{r}\nabla_S(V_{int} + V_{ext}), \tag{2}$$

where ∇_S is the surface gradient, which in spherical coordinates is defined as:

$$\nabla_S = \hat{\theta}\frac{\partial}{\partial\theta} + \hat{\phi}\frac{1}{\sin\theta}\frac{\partial}{\partial\phi}, \tag{3}$$

where $\hat{\theta}$ and $\hat{\phi}$ are the unit vectors oriented in the direction of increasing colatitude and longitude, respectively. Although the radial component of the data is not used to derive the model, some of the corresponding equations for the radial magnetic field are also given hereunder as they will be used further on in Section 5. The radial component of the magnetic field is written as:

$$B_r = -\frac{\partial}{\partial r}(V_{int} + V_{ext}). \tag{4}$$

Now, assuming that the magnetic field $\vec{B}_{int}$ is induced in the conductive Earth by the time-varying primary magnetic field $\vec{B}_{ext}$, the two potentials V_{int} and V_{ext} can be expanded in real spherical harmonics as follows:

$$V_{ext} = a\sum_{lm}\left(\frac{r}{a}\right)^{l}\left[q_l^m(t)Y_l^{m,(c)}(\theta,\phi) + s_l^m(t)Y_l^{m,(s)}(\theta,\phi)\right], \tag{5}$$

and

$$V_{int} = a\sum_{lm}\left(\frac{a}{r}\right)^{l+1}\left[g_l^m(t,\sigma)Y_l^{m,(c)}(\theta,\phi) + h_l^m(t,\sigma)Y_l^{m,(s)}(\theta,\phi)\right], \tag{6}$$

where $Y_l^{m,(c)}$ and $Y_l^{m,(s)}$ are the Schmidt quasi-normalized real spherical harmonics (Winch et al., 2005), $\sum\limits_{lm}$ is the shorthand notation for $\sum\limits_{l=1}^{L}\sum\limits_{m=0}^{l}$, l, m, and L are the spherical harmonic degree, order and truncation degree, respectively, q_l^m and s_l^m are the expansion coefficients of the external field, g_l^m and h_l^m are the expansion coefficients of the internal (induced) field, and $a = 6{,}371.2$ km is the Earth's reference radius. Note that the coefficients g_l^m and h_l^m depend on the Earth conductivity σ. Now, using Equations 2, 4, 5, and 6, the horizontal component $\vec{B}_H$ and the radial component B_r of the magnetic field may be expressed as:

$$\begin{aligned}\vec{B}_H = &-\sum_{lm}\left(\frac{r}{a}\right)^{l-1}\left[q_l^m(t)\nabla_S Y_l^{m,(c)}(\theta,\phi) + s_l^m(t)\nabla_S Y_l^{m,(s)}(\theta,\phi)\right],\\ &-\sum_{lm}\left(\frac{a}{r}\right)^{l+2}\left[g_l^m(t,\sigma)\nabla_S Y_l^{m,(c)}(\theta,\phi) + h_l^m(t,\sigma)\nabla_S Y_l^{m,(s)}(\theta,\phi)\right],\end{aligned} \tag{7}$$

and

$$\begin{aligned} B_r = &-\sum_{lm} l\left(\frac{r}{a}\right)^{l-1}\left[q_l^m(t)Y_l^{m,(c)}(\theta,\phi)+s_l^m(t)Y_l^{m,(s)}(\theta,\phi)\right] \\ &+\sum_{lm}(l+1)\left(\frac{a}{r}\right)^{l+2}\left[g_l^m(t,\sigma)Y_l^{m,(c)}(\theta,\phi)+h_l^m(t,\sigma)Y_l^{m,(s)}(\theta,\phi)\right]. \end{aligned} \tag{8}$$

3.2. Model Derivation

The model is derived by assuming that the Earth's surface is a sphere of radius $r = a$ and the ground magnetic data are all located on that sphere. Since only the horizontal component is used, the equations corresponding to the radial component are omitted in this section. At the Earth's surface, Equation 7 may be expressed as:

$$\vec{B}_{H,r=a} = -\sum_{lm}\left[q_l^m(t)+g_l^m(t,\sigma)\right]\nabla_S Y_l^{m,(c)}(\theta,\phi)+\left[s_l^m(t)+h_l^m(t,\sigma)\right]\nabla_S Y_l^{m,(s)}(\theta,\phi), \tag{9}$$

where $\vec{B}_{H,r=a}$ is the horizontal component of a ground magnetic measurement. If one assumes a 1D conductivity—that is σ only depends on the radius r—the internal coefficients may be further expressed as a function of the inducing external coefficients (Grayver et al., 2021; Kruglyakov et al., 2022) such as:

$$g_l^m(t,\sigma) = \int_0^{\infty} Q_l(\tau,\sigma)q_l^m(t-\tau)d\tau \approx \int_0^{T} Q_l(\tau,\sigma)q_l^m(t-\tau)d\tau, \tag{10}$$

and

$$h_l^m(t,\sigma) = \int_0^{\infty} Q_l(\tau,\sigma)s_l^m(t-\tau)d\tau \approx \int_0^{T} Q_l(\tau,\sigma)s_l^m(t-\tau)d\tau, \tag{11}$$

where Q_l is called the Q-kernel corresponding to the spherical harmonic degree l, and T is a time taken large enough for the right-hand sides of Equations 10 and 11 to be good approximations. Following Kruglyakov et al. (2022), T is set to 6 months. The coefficients q_l^m and s_l^m are evaluated at discrete times $t_k = k\Delta t$, where k is a positive integer and the time step Δt is set to 1 hour. For a certain time t_k, if we assume that the external coefficients q_l^m and s_l^m are known at all times between $t_k - N\Delta_t$ and t_k, where N is chosen such that $N\Delta_t$ is equal to 6 months, then the corresponding induced coefficients g_l^m and h_l^m may be estimated at t_k by approximating the right-hand side of Equations 10 and 11 using the following weighted sums (Kruglyakov et al., 2022):

$$\begin{aligned} g_l^m(t_k,\sigma) &\approx \sum_{n=0}^{N_k} W_l^n q_l^m(t_k - n\Delta_t) \\ &= W_l^0 q_l^m(t_k) + \sum_{n=1}^{N_k} W_l^n q_l^m(t_k - n\Delta_t), \end{aligned} \tag{12}$$

and

$$\begin{aligned} h_l^m(t_k,\sigma) &\approx \sum_{n=0}^{N_k} W_l^n s_l^m(t_k - n\Delta_t) \\ &= W_l^0 s_l^m(t_k) + \sum_{n=1}^{N_k} W_l^n s_l^m(t_k - n\Delta_t), \end{aligned} \tag{13}$$

where the summation superscript N_k is equal to $\min(k-1, N)$ and accounts for the fact that the time series of external coefficients q_l^m and s_l^m are finite, and W_l^n are the weights. The methodology to compute the weights is described in Appendices A and B of Kruglyakov et al. (2022). Substituting g_l^m and h_l^m from Equations 12 and 13 in Equation 9 yields:

$$\begin{aligned} &\vec{B}_H(t_k, r=a) + \sum_{lm}\sum_{n=1}^{N_k} W_l^n\left[q_l^m(t_k - n\Delta_t) + s_l^m(t_k - n\Delta_t)\right]\nabla_S Y_l^{m,(c)}(\theta,\phi), \\ &= -\sum_{lm} q_l^m(t_k)\left[1+W_l^0\right]\nabla_S Y_l^{m,(c)}(\theta,\phi) + s_l^m(t_k)\left[1+W_l^0\right]\nabla_S Y_l^{m,(s)}(\theta,\phi). \end{aligned} \tag{14}$$

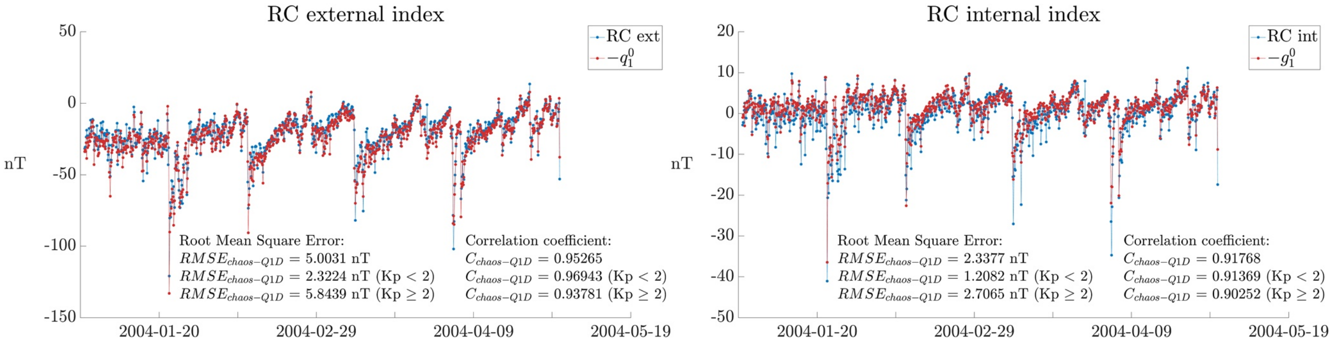

Figure 2. Comparison between the external RC index and minus the external coefficients q_1^0 (left panel) and between the internal RC index and minus the internal coefficients g_1^0 (right panel) of the degree 1 model from 1 January 2004 to 31 April 2004. The root-mean-square error (RMSE) and the correlation coefficient (CC) for the full 4-month period, at times when Kp < 2, and at times when Kp ≥ 2, are given at the bottom of each panel.

Note that the left-hand side of Equation 14 only depends on the external coefficients q_l^m and s_l^m at the times $t_k - n\Delta t$, with $1 \leq n \leq N$, whereas the right-hand side only depends on these same coefficients at the time t_k. If one assumes that the external coefficients are known at all timesteps between $t_k - \Delta t$ and $t_k - N\Delta t$, then one can find an estimate of the model coefficients at t_k by solving the following minimization problem:

$$\min_{\vec{m}} \quad \left(\vec{D} - \mathbf{G}\vec{m}\right)^T \mathbf{C}_\mathbf{d}^{-1}\left(\vec{D} - \mathbf{G}\vec{m}\right) \tag{15}$$

where $\vec{D}$ is the corrected data vector which can be computed using the left-hand side of Equation 14, $\vec{m}$ is the parameter vector containing the external coefficients q_l^m and s_l^m at the time t_k, $\mathbf{G}$ is a matrix such that $\mathbf{G}\vec{m}$ is the model prediction, and $\mathbf{C}_\mathbf{d}^{-1}$ is the a priori diagonal data covariance matrix for which we take all diagonal elements equal to 1 nT^{-2}. Solving the minimization problem 15 for each timestep t_k provides hourly time series of estimates of the external coefficients q_l^m and s_l^m. In this study, this is done between 1997 and 2022 using the preprocessed ground magnetic data presented in Section 2. The least-square, unregularized solution of the problem in 15 may be expressed as:

$$\vec{m}^{\,est} = \left(\mathbf{G}^\mathbf{T}\mathbf{G}\right)^{-1}\mathbf{G}^\mathbf{T}\vec{D}. \tag{16}$$

where $\vec{m}^{\,est}$ is the least-square estimate of $\vec{m}$ at t_k. It is computed for three different truncation degrees: $L = 1$, $L = 2$, and $L = 3$. We thus obtain three versions of the model with three different truncation degrees. In a second step, the corresponding time series for the internal coefficients g_l^m and h_l^m can be computed using Equations 12 and 13.

The models presented in this paper are not regularized. In the initial phases of this project, we tested various regularization strategies in an attempt to minimize contamination by un-modeled ionospheric fields. For example, one strategy consisted of minimizing the North-South asymmetry of the field with respect to the magnetic equator in CD coordinates. Another strategy involves smoothing the field far above the ionosphere at several Earth radii. However, neither of these strategies was successful in minimizing ionospheric field contamination.

4. Comparison With the RC, Dst, and Dcx Indices

The activity level of the magnetospheric field has been historically monitored using the Dst index, derived using hourly data from 4 ground magnetic observatories (Sugiura, 1963). This index represents the intensity of the horizontal component of the disturbance magnetospheric field at the dipole equator and has been further separated into its external and induced components using an a priori conductivity model (Maus & Weidelt, 2004). It is known, however, to be affected by several problems, such as an improper data preprocessing (Mursula et al., 2008, 2011) and an unstable baseline during geomagnetic quiet times (Lühr & Maus, 2010; Olsen et al., 2005). To address these issues, some improved indices have been developed. The Dxt and Dcx indices (Karinen & Mursula, 2006; Mursula et al., 2008, 2011; Mursula & Karinen, 2005) were derived using an improved data normalization and are corrected from a slowly varying "non-storm component." A separate effort was devoted to the development of the RC index as part of the CHAOS geomagnetic model series (Olsen et al., 2014). The RC index was shown to have a more stable baseline than the Dst index. It is computed using an hourly spherical harmonics analysis of hourly vector data from 21 ground observatories and, similarly to the Dst, is separated in its external and induced components. In this section, we check that the model derived in this paper is consistent with the RC index, as this index is computed with a methodology similar with the one used to derive our model. We also comment on the comparison with the original Dst index, as well as with the corrected Dcx index.

Table 1
Root-Mean-Square Errors (RMSE) in nT and Correlation Coefficients (CC) Between the External RC Index and Minus the Coefficient q_1^0 of the Degree 1 Model From 1 January 1997 to 31 December 2022

	External		Internal	
	RMSE	CC	RMSE	CC
Full period	4.5808	0.9675	2.0225	0.9252
Quiet times (Kp < 2)	2.3367	0.9745	1.1609	0.9022
Active times (Kp ≥ 2)	6.5081	0.9550	2.8048	0.9159

Figure 2 shows a comparison between the time series of the external and internal RC indices disseminated as part of the latest CHAOS model release, and $-q_1^0$ and $-g_1^0$, the degree 1 and order 0 external and internal coefficients of the degree 1 model derived as described in Section 3. The comparison is shown from 1 January 2004 to 31 April 2004. A minus sign was added to the model coefficients to be consistent with the convention chosen for the RC index (Olsen et al., 2014). The two panels of Figure 2 show that the $-q_1^0$ and $-g_1^0$ coefficients are in good agreement with the external and internal RC indices on the considered period. This is well representative of what can be observed at all times between 1997 and 2022.

The Root-Mean-Square Error (RMSE) and the Correlation Coefficient (CC) are also provided at the bottom of each panel. Both quantities are computed for the full 4-month period, as well as for two subperiods corresponding to geomagnetic quiet times, defined as times when the Kp index (Matzka et al., 2021) is less than 2, and geomagnetic moderate and active times, defined as times when the Kp index is greater than or equal to 2. The correlation coefficient is greater than 0.9 for all levels of geomagnetic activity and for both external and internal coefficients, indicating a strong positive correlation between the RC indices and the order 0 coefficients of our degree 1 model. The RMSE between external (resp. internal) coefficients varies from 2.3 nT (resp. 1.2 nT) for quiet geomagnetic times to 5.8 nT (resp. 2.7 nT) for active geomagnetic times. The values at quiet times show that the model baseline is consistent with that of RC, suggesting that our model is not affected by any significant baseline instability. The differences between our model and RC increase for active geomagnetic conditions but remain well below the amplitude of the magnetospheric field signal. Such differences are attributed to the different data sets and methodological approaches used to derive the RC index and the degree 1 model.

The RMSEs and CCs for the full data set, from 1997 to 2022, are provided in Table 1. The CCs never drop below 0.9, and all RMSE values are within 1 nT of those in Figure 2. The values in Table 1 confirm the results obtained in Figure 2.

We also performed similar comparisons between the original Dst and corrected Dcx indices, and minus the total degree 1 and order 0 coefficient of our degree 1 model. These comparisons are done between 1 January 2000 and 31 December 2014, which is the period covered by the definitive version of the Dcx index computed with data from 17 magnetic observatories. The results are shown in Table 2 together with the corresponding results for the total RC index. While also consistent with our model, the Dst and Dcx indices generally show a less good agreement than the RC index. This is particularly true for geomagnetic quiet times, where the RMSE raises to 6.3 nT (resp. 7.4 nT) for the Dst index (resp. the Dcx index), whereas it is lower for the RC index, around 3 nT. Additionally, the correlation coefficients drop to 0.87 and 0.81 for the Dst and Dcx indices, respectively. These results reflect some substantial differences in the quiet-time baselines between the Dst and Dcx indices on one hand, and the RC index and our model on the other. It is already known that the Dst index suffers from baseline instabilities during geomagnetic quiet times. Further investigations are needed to better understand the reasons of this discrepancy.

Table 2
Root-Mean-Square Errors (RMSE) in nT and Correlation Coefficients (CC) Between the Total Dst, Dcx and RC Indices and Minus the Coefficient v_1^0 of the Degree 1 Model From 1 January 2000 to 31 December 2014

	RMSE			CC		
	Dst	Dcx	RC	Dst	Dcx	RC
Full period	7.5375	9.4111	6.1559	0.9461	0.9298	0.965
Quiet times (Kp < 2)	6.2666	7.3762	2.9734	0.8682	0.8084	0.9712
Active times (Kp ≥ 2)	8.9517	11.5747	8.7473	0.9540	0.9451	0.9537

5. Model Validation and Performance Assessment Using Satellite Data

The model is further validated by comparing it to independent satellite magnetic data from the Swarm constellation (Friis-Christensen et al., 2006), the CHAMP satellite (Reigber et al., 2002) and the Ørsted satellite (Neubert et al., 2001). This can be achieved by computing the model predictions at satellite altitudes using Equations 7 and 8. Such a comparison provides additional insights on at least two specific aspects. The first one is that, in contrast with the observatory data used as input to the model, the several years of satellite data used in this study provide much better coverage of all geographic sectors at all local times for quiet and moderate geomagnetic activity levels. This allows testing the model in both poorly sampled and relatively better sampled geographic sectors (see Figure 1). This is not the case for high geomagnetic activity levels, however, as these periods of time are fewer and shorter (Love et al., 2015; Yokoyama & Kamide, 1997)—typically several hours to a few days. During active geomagnetic times, the geographic and local time satellite data coverage is much sparser.

The second benefit of using satellite data is that such data were collected above most ionospheric magnetic field sources. The model, however, was built assuming that the only primary magnetic fields in ground data are external fields, and the only internal magnetic fields are secondary induced fields, as expressed in Equation 7. This assumption doesn't hold at satellite altitudes for any residual ionospheric field contaminating the model, which could lead to substantial discrepancies between model predictions and satellite data. The comparison with satellite data is thus expected to provide insights into possible model contamination by residual ionospheric magnetic fields. The same reasoning, however, cannot be applied to possible model contamination by magnetic fields generated in the outer magnetosphere, as these fields are produced by sources above satellite altitudes.

5.1. Satellite Data Preprocessing

We use 1 Hz vector magnetic data from Swarm Alpha and Bravo between 1 January 2014, and 31 December 2021, from CHAMP between 20 July 2000, and 17 September 2010, and from Ørsted between 20 July 2000, and 6 December 2005. All these satellites were launched on near-polar orbits. During the considered periods of time, Swarm Alpha and Bravo orbited on nearly circular orbits at average altitudes of 460 and 530 km, respectively, and CHAMP orbited on a nearly circular orbit at an average altitude of 450 km. Ørsted orbited at higher altitudes, on an elliptic orbit with an apogee of 865 km and a perigee of 650 km. The local time planes of all three satellites slowly drifted such that Swarm and CHAMP covered all local times in approximately 4 months, and Ørsted covered all local times in approximately 27 months.

The satellite data are preprocessed in the following way. Obvious outliers are first removed using the median absolute deviation technique in a 10 s running window with a threshold value equal to four times the absolute median deviation in each window, and the data are subsequently resampled every minute. CHAMP data are further selected by retaining data only when attitude information is provided by both star cameras. For consistency with the preprocessing of ground data (cf. Section 2), satellite data are corrected for the core field, the lithospheric field, the magnetospheric field originating outside the inner magnetosphere (expressed in GSM coordinates) and its induced counterpart using the CHAOS-7.15 model, and the climatological part of the E-region ionospheric primary and induced fields using the DIFI model. The data are selected between 5 and 55° quasi-dipole latitudes in both hemispheres.

Figure 3 presents the data distribution for each satellite mission—the data from the Swarm satellites Alpha and Bravo are considered together—and several geomagnetic activity levels after the data preprocessing and selection. The four geomagnetic activity levels in this figure are defined using ranges of the Hp30 magnetic index (Yamazaki et al., 2022), which provides a proxy of the global geomagnetic activity every 30 min in units of thirds of nT. The Hp30 index is more appropriate for satellite data than the traditional Kp index due to its improved time resolution. For Hp30 < 6, Swarm Alpha and Bravo provide by far the best data coverage, while CHAMP and Ørsted provide more uneven coverage. Ørsted, in particular, has sparser coverage for 06:00 and 18:00 local times. For Hp30 ≥ 6, the data coverage of all satellites is much sparser, and CHAMP provides the best data coverage.

5.2. Terminology and Preliminary Comments

The preprocessed satellite data are compared to the three versions of the model derived in Section 3, that is, the degree 1, 2 and 3 models. In the following, these models will be referred to as "L1," "L2," and "L3" models, respectively. The same satellite data are also compared to the Solar Magnetic (SM) part of the external field component of the CHAOS-7.15 model, which represents the inner magnetospheric field in SM coordinates

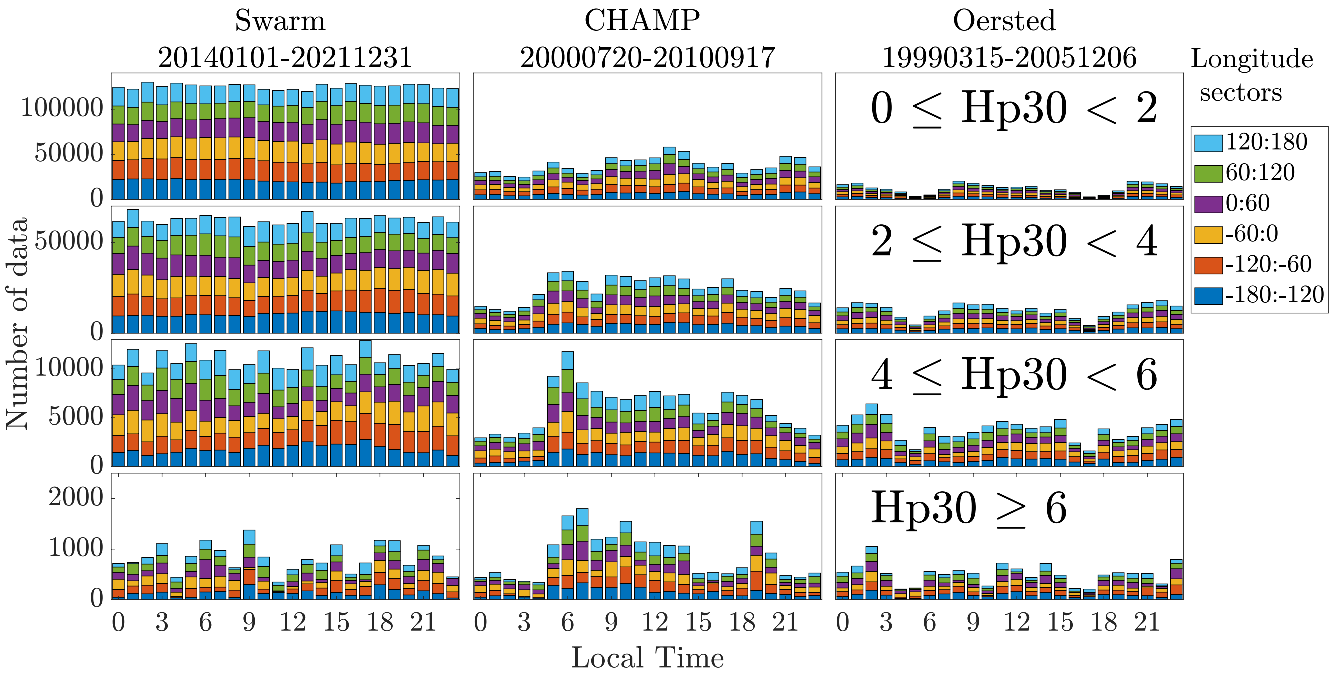

Figure 3. Histograms showing the distributions in local time and longitude of Swarm Alpha and Bravo (left column), CHAMP (middle column) and Ørsted (right column) data after data preprocessing and selection. The distributions are given for four geomagnetic activity levels defined using ranges of the Hp30 index: $0 \le \mathrm{Hp30} < 2$ (first row), $2 \le \mathrm{Hp30} < 4$ (second row), $4 \le \mathrm{Hp30} < 6$ (third row) and $\mathrm{Hp30} \ge 6$ (fourth row). The x-axis of each histogram gives the local time between 0 and 24, in steps of one hour, and the color code gives the longitude from −180° to 180° in steps of 60°.

(Equations 2a, 2b and 2c in Finlay et al. (2020)). Note that the SM part of the external component of the CHAOS-7.15 model was the only part of the CHAOS-7.15 model that was not removed from the data in Section 3.2. This model is referred to as the "CHAOS-7.15 SM" model and is used here as a benchmark.

Before proceeding to the model comparison, let us make some preliminary comments. First, the L1, L2, and L3 models are computed from the exact same data set and using the same methodology. They only differ by their truncation degree (noted L in Section 3). Therefore, any difference in performance is attributed to different spatial resolutions.

Second, hourly variations of the symmetric component can be tracked by all models, whatever their truncation, whereas hourly variations of the asymmetric component can only be tracked by the L2 and L3 models. In the CHAOS-7.15 SM model, the symmetric component is tracked by the RC index (see Equation 3 in Finlay et al. (2020)). The degree 2 spherical harmonics in CHAOS-7.15 SM are static and therefore cannot account for hourly variations, unlike the L2 and L3 models. Note that the L2 and L3 models also account for a static asymmetric field. Table 3 summarizes the ability of each model to track hourly variations of the symmetric and asymmetric components.

Third, CHAOS-7.15 SM is expected to properly separate magnetospheric and ionospheric fields when considering long-term average or climatological variations of these fields. Such a separation, however, cannot be achieved in hourly variations using satellite data, as satellite data do not provide sufficient geographical coverage on hourly time scales. On the other hand, models based on ground data only are able to track hourly variations thanks to the superior local time coverage of ground data, but the separation of the ionospheric and magnetospheric fields in these models is difficult to achieve.

Table 3
Simplified Overview of the Ability of the L1, L2, L3, and CHAOS-7.15 SM Models to Track Hourly Variations of the Symmetric and Asymmetric Components of the Near-Earth Magnetic Field Generated in the Inner Magnetosphere

	CHAOS-7.15 SM	L1	L2	L3
Hourly variations of the symmetric field (degree 1 SH)	✓	✓	✓	✓
Static asymmetric field (degree 2 SH)	✓		✓	✓
Hourly variations of the asymmetric field (degree 2 SH)			✓	✓
Hourly variations of the asymmetric field (degree 3 SH)				✓

Finally, it is worth noting that, while the Swarm, CHAMP and Ørsted data sets are completely independent from the data sets used to build L1, L2, and L3, they overlap with the data set used to derive CHAOS-7.15 SM (Finlay et al., 2020).

5.3. Model Performance Metrics

We use two metrics to evaluate the performances of the CHAOS-7.15 SM, L1, L2, and L3 models with respect to satellite data. The first metric is the root mean square error (RMSE) between the satellite data and the model predictions. The RMSE is computed independently for each vector component in spherical coordinates as:

$$\mathrm{RMSE}_\alpha = \left(\frac{1}{N} \sum_{i=1}^{N} \left[B^{(i)}_{\alpha,\mathrm{data}} - B^{(i)}_{\alpha,\mathrm{model}} \right]^2 \right)^{\frac{1}{2}}, \qquad \alpha \in \{r, \theta, \phi\}, \tag{17}$$

where $B^{(i)}_{\alpha,\mathrm{data}}$ (resp. $B^{(i)}_{\alpha,\mathrm{model}}$) is the i-th satellite data (resp. model prediction) on each component, and N is the total number of data.

Before computing the RMSEs, each coefficient time series is interpolated linearly to obtain the same 1-min resolution as the satellite data. The RMSE is computed independently for various geomagnetic activities, characterized by the Hp30 index (Yamazaki et al., 2022). The data are binned according to the level of geomagnetic activity and the satellite mission—the data from Swarm Alpha and Bravo are binned together. In each data bin, we reject data outside the 0.997 quantile, which efficiently removes any remaining outliers while allowing sufficient data variability at all geomagnetic activity levels. Finally, the RMSEs are computed from the data in each bin for each model and component.

We also measure the relative performance of each model compared to the others. To do so, we choose a reference model, L1, and calculate the relative difference (RD) of each model with respect to L1

$$\mathrm{RD}_{\alpha,\mathrm{model}} = \frac{\mathrm{RMSE}_{\alpha,\mathrm{L1}} - \mathrm{RMSE}_{\alpha,\mathrm{model}}}{\mathrm{RMSE}_{\alpha,\mathrm{L1}}} \times 100, \qquad \alpha \in \{r, \theta, \phi\}, \tag{18}$$

the subscript model can be either CHAOS-7.15 SM, L2 or L3. Each element in RD measures (in percent) the relative improvement (positive values) or deterioration (negative values) on the corresponding component of the fit to satellite data of each model compared to the fit of the L1 model to the same data.

5.4. Comparison With Swarm Data

The CHAOS-7.15 SM, L1, L2, and L3 models are first compared with Swarm data. The left column of Figure 4 shows the RMSEs for the four models as a function of the Hp30 index for the south, east and radial components. In this figure, the lower the RMSE, the better the fit of the model to Swarm data. As a first observation, the RMSE increases monotonically as a function of Hp30 for all models and components. This implies that the model is in better agreement with Swarm data during quiet geomagnetic times compared to active geomagnetic times. It may be explained in part by the different time resolutions of the Swarm data and of the model coefficient time series. The 1-min Swarm data are indeed more likely to capture fast variations of the magnetospheric field during active geomagnetic times than model predictions from linearly interpolated hourly coefficients. Another possible explanation is the imperfect correction of fast-varying ionospheric fields by the DIFI model. The DIFI model was inferred from quiet-time magnetic field data and is not expected to accurately represent ionospheric field variations during geomagnetically active times when such variations can significantly deviate from their quiet-time configuration (Yamazaki & Maute, 2017). As stated in Section 5.2, any residual ionospheric field is expected to increase discrepancies between model predictions and satellite data.

The results presented in the left column of Figure 4 show that the RMSEs between L2 and L3 and Swarm data are roughly 5–20 nT smaller than the RMSEs for CHAOS-7.15 SM and L1 on all three components during active geomagnetic times, defined here as times when Hp30 ≥ 4. Additionally, the L2 and L3 curves are close to one another, as are the CHAOS-7.15 SM and L1 curves, which means that L2 and L3 have comparable performances at these geomagnetic activity levels, and the same for CHAOS-7.15 SM and L1. The figures in the right column of Figure 4 show that L2 and L3 fit Swarm data about 10%–20% better than L1 and CHAOS-

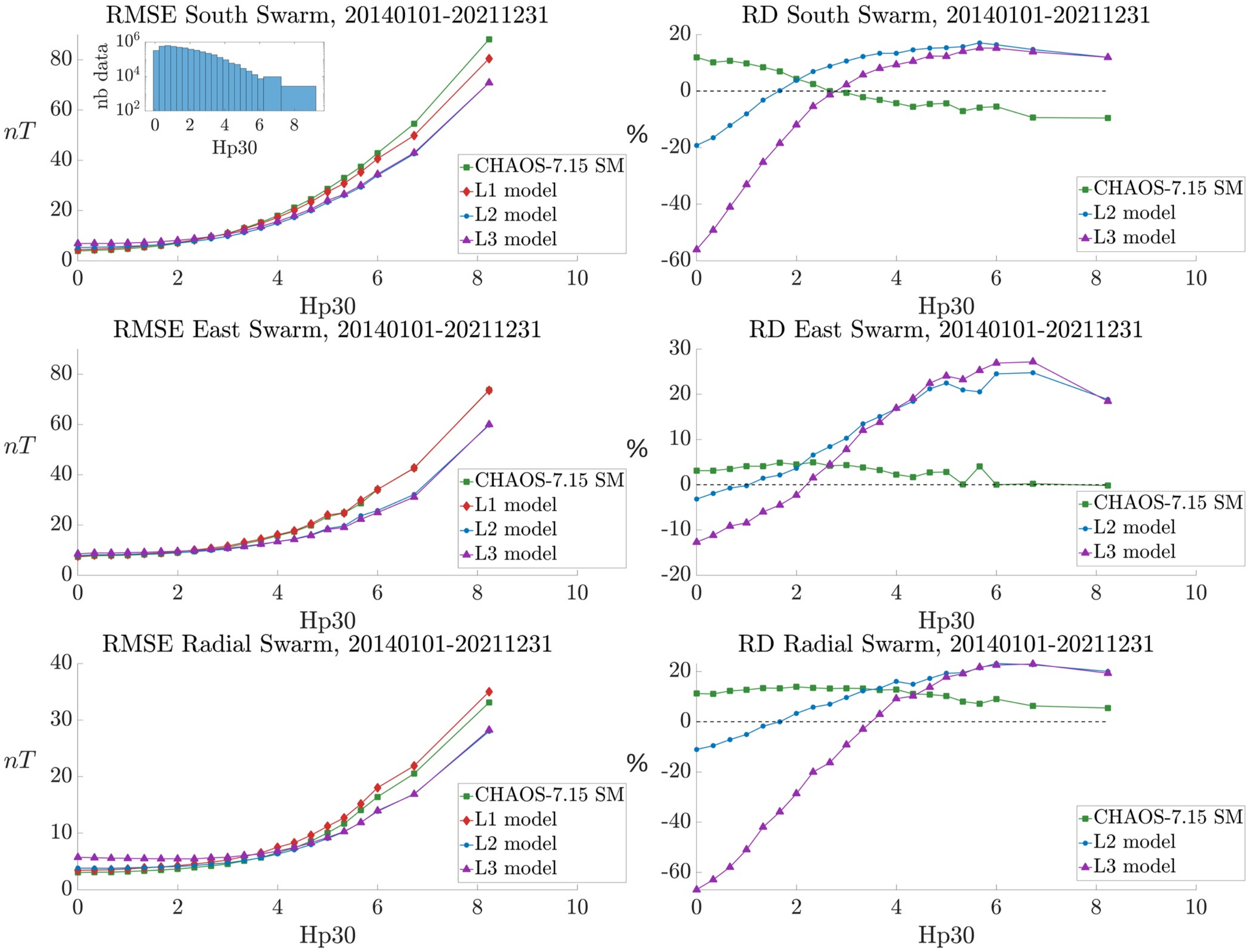

Figure 4. (Left column) RMSE between Swarm data and CHAOS-7.15 SM (green squares), L1 (red diamonds), L2 (blue dots) and L3 (purple triangles) as a function of geomagnetic activity as described by the Hp30 index and for the south (first row), east (second row) and radial (third row) components. (Right column) The relative difference expressed in % between the RMSE of CHAOS-7.15 SM (green squares), L2 (blue dots) and L3 (purple triangles) and the RMSE of L1 (red diamonds in the left column) for the south (first row), east (second row) and Radial (third row) components as a function of the Hp30 index. The histogram in the upper left panel shows the number of data in each Hp30 bin.

7.15 SM when Hp30 ≥ 4. This suggests that the higher degree and order magnetospheric field models are able to capture a larger portion of the overall magnetospheric field and its induced counterpart during active geomagnetic times.

The situation in the left column of Figure 4 is less clear for quiet and moderate geomagnetic times, defined here as times when Hp30 < 4, as all curves are very close to each other. The relative differences shown in the right column of Figure 4 are helpful in that regard.

For Hp30 < 2 (resp. 2 ≤ Hp30 < 4), the fit of CHAOS-7.15 SM to Swarm data is 5%–10% better than (resp. roughly equal to) the fit of L1 on the south and east components. On the radial component, the fit of CHAOS-7.15 SM is 5%–10% better at all Hp30 values lower or equal to 4. The slightly better performance of CHAOS-7.15 SM compared to L1 during quiet and moderate geomagnetic times may be attributed to the fact that, unlike L1, CHAOS-7.15 SM includes a static degree 2 representation of the asymmetric component of the field. The better performances of the CHAOS-7.15 SM model on the radial component could also be related to the fact that this component of the data was used to constrain CHAOS-7.15 SM (Finlay et al., 2020).

During moderate geomagnetic times, when 2 ≤ Hp30 < 4, L2 fits Swarm data better than L1 on all three components (up to roughly 20%) and better than CHAOS-7.15 SM on the south and east components; it fits

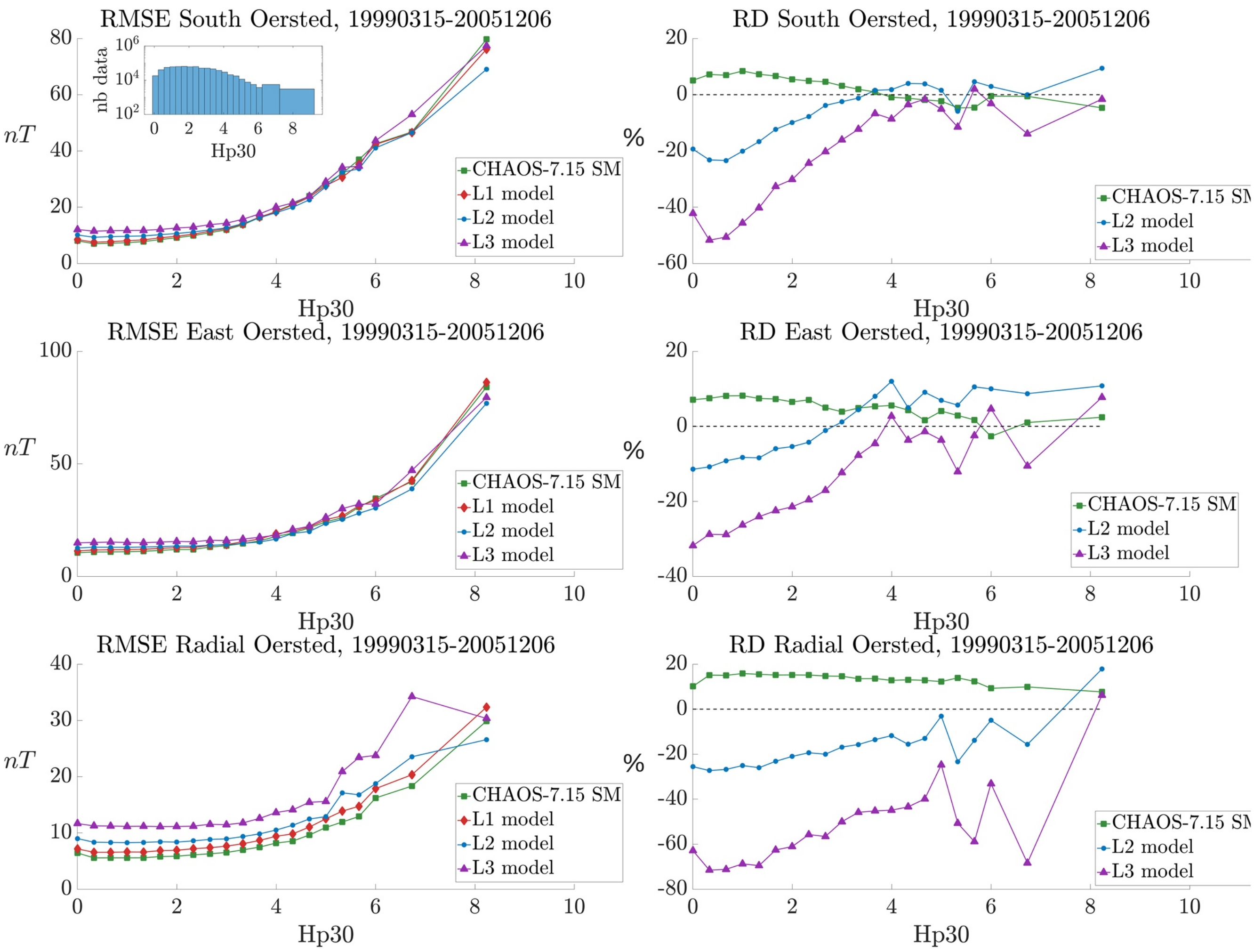

Figure 5. Same as Figure 4 for the CHAMP satellite data.

the data less well than CHAOS-7.15 SM on the radial component. However, L3 generally fits Swarm data less well than L2, suggesting that no additional information was gained by increasing the degree and order of the model.

During quiet geomagnetic times, when Hp30 < 2, both L2 and L3 fit Swarm data less well than L1 on all three components, especially on the south and radial components. Furthermore, the fit of L3 is worse than the fit of L2, confirming what was observed at moderate geomagnetic times. A possible explanation may lie in the heterogeneous and, in some areas, geographically sparse ground data coverage (see Section 2). Increasing the spatial resolution may lead to spurious oscillations in the model due to a lack of ground data in some areas, whereas Swarm data provide much better geographical coverage for the model validation (see Figure 3). Model contamination by ionospheric fields is also a good candidate to explain the degradation of the fit to Swarm data when increasing the spatial resolution. To test the validity of this statement, a similar figure to Figure 4 was produced—shown in the Supporting Information S1—where ionospheric fields were not corrected using the DIFI model in both the ground data used to derive the L1, L2 and L3 models (cf. Section 2) and the Swarm data (cf. Section 5.1). The obtained L2 and L3 fit Swarm data less well than the L2 and L3 with DIFI correction during quiet geomagnetic times, thus supporting our hypothesis that unmodeled ionospheric fields can leak into L1, L2 and L3 during quiet geomagnetic times.

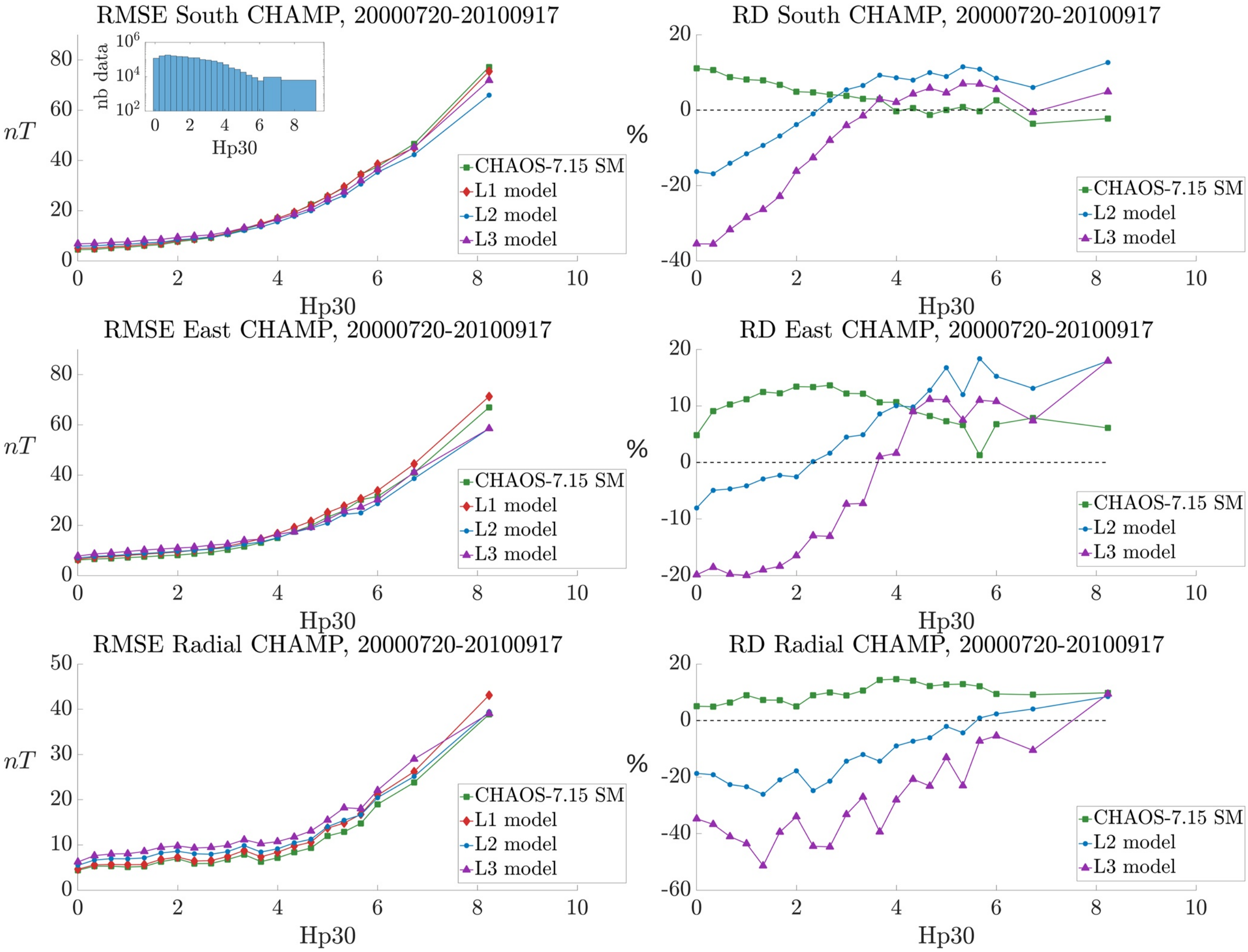

Figure 6. Same as Figure 4 for the Ørsted satellite data.

5.5. Comparison With CHAMP and Ørsted Data

We next test if the results obtained with Swarm data in Section 5.4 can be confirmed using CHAMP and Ørsted data. Note that CHAMP and Ørsted data do not provide as good a spatial and temporal coverage as Swarm data (cf. Section 5.1), which could lead to differences in the results. It is also worth mentioning that Swarm, CHAMP and Ørsted orbit at different altitudes, with potential implications for model differences when a model is contaminated by ionospheric fields.

The results for CHAMP data (Figure 5) mostly confirm what was obtained with Swarm data, with one noticeable difference. While L2 fits CHAMP data better than L1 when Hp30 ≥ 2 on the south and east components, this is no longer the case on the radial component. Unlike what was observed with Swarm data, L2 fits CHAMP data less well than L1 when Hp30 < 6 on the radial component. Compared to CHAOS-7.15 SM, L2 performs better when Hp30 ≥ 4 on the south and east components and less well for all Hp30 values on the radial component. We don't have an explanation at the moment for this puzzling result other than perhaps the degraded local time coverage of CHAMP data compared to Swarm data. The CHAMP results also confirm that increasing the spatial resolution to degree and order 3 deteriorates the fit to satellite data.

The results obtained with Ørsted data, shown in Figure 6, confirm the orders of magnitude and general trends of the RMSEs. However, they are noisier, probably due to the degraded spatial and temporal coverage of Ørsted data compared to Swarm and CHAMP data. Also, L2 doesn't fit Ørsted data better than L1 when Hp30 ≥ 4, except on the east component. This could possibly be attributed to the higher altitude of the Ørsted satellite, which could enhance the effects of ionospheric field contamination, as discussed earlier.

6. Discussion

The results presented in Section 5 show that the degree 2 model—also termed the L2 model—improves the fit to satellite data for moderate and high geomagnetic activity levels on the south and east components. The question now remains of what is the morphology of the field predicted by this model, and in particular, whether the improved fit to satellite data during moderate and active geomagnetic times is associated with a better representation of magnetospheric local time asymmetries. Information on such asymmetries could be used to better constrain storm-time magnetospheric electric currents, in both case studies of storms and substorms and statistical studies (Haaland & Gjerloev, 2013; Lühr & Zhou, 2020a; Ohtani, 2021; Ohtani et al., 2021). Also of interest is to investigate why the fit of the degree 2 model to satellite data is not improved for quiet geomagnetic times, a question relevant to geomagnetic field modeling. In this section, we discuss the local time structure of the field predicted by the degree 2 model for all geomagnetic activity levels. We first look at the average local time asymmetry over 25 years as a function of geomagnetic activity in Section 6.1 and discuss the potential contamination of the degree 2 model by ionospheric fields. In Section 6.2, we then use the degree 2 model to discuss the local time structure of the field during two geomagnetic storms.

6.1. Average Local Time Asymmetry Over 25 years

In a previous study, Lühr and Zhou (2020b) could identify the average near-Earth magnetospheric field local time asymmetry over 5 years in the residuals between data from the CHAMP satellite and the CHAOS-6 model. Their analysis was limited to nighttime and Kp values below 4.7. Consistently with some other studies on storm-time near-Earth magnetospheric field (Le et al., 2011; Love & Gannon, 2010), this average asymmetry was found to be dawn-dusk oriented—see Figure 4 of Lühr and Zhou (2020b). Lühr and Zhou (2020b) clearly showed that local time asymmetries could produce substantial errors in data-based geomagnetic field models, such as the CHAOS model series. Furthermore, it was noted that the field becomes more asymmetric with increasing values of Kp and that no clear asymmetry could be observed for Kp values below roughly 2. In what follows, we investigate if our degree 2 model can reproduce these earlier results on a much longer time period, and what new insights our model can provide on the local time asymmetry at higher geomagnetic activity levels.

Figure 7 shows averages over 25 years of the asymmetric part of the south component of the total, primary and induced magnetospheric magnetic fields as predicted by the degree 2 model and as a function of SM magnetic local time (SMLT) and Hp30. Here, SMLT is defined as $(180 - \phi_{SM})/15$, where ϕ_{SM} is the longitude in SM coordinates. The averages were calculated along the magnetic equator in CD coordinates and at the Earth's surface (assumed spherical) in the following way. For every 1 hr time step between 1 January 1997, and 31 December 2022, the asymmetric part of the south component of the field was computed every 15° at the magnetic equator in CD coordinates from the non-zonal terms ($m \neq 0$ in Equation 7). In the second step, the data was sorted in 1-hr SMLT and Hp30 bins. The average asymmetric field was then computed by taking the mean in each bin. In Figure 7, the obtained averages are represented in two complementary ways. In the left column, they are shown in color-coded 2D graphs as a function of Hp30 and SMLT. In the right column, they are shown as SMLT profiles for various geomagnetic activity levels.

The upper left graph in Figure 7 is in the same format as Figure 4 of Lühr and Zhou (2020b) extended to all local times and up to Hp30 9. The portion of this figure delimited by black lines can be compared to Figure 4 of Lühr and Zhou (2020b). Note that the *y*-axis in these two figures is in opposite directions. Furthermore, it should be stressed that these two figures do not represent the exact same signal. The static, external SM component of the CHAOS-6 model—Equations (2a)–(2c) in Finlay et al. (2020)—was subtracted from the data used to build Figure 4 of Lühr and Zhou (2020b), whereas the static, external SM component of the CHAOS-7.15 model was not subtracted from the ground data used to compute our degree 2 model. However, the resulting difference is expected to be small as the static, external SM component in CHAOS models is of the order of a few nT at most.

The average dawn-dusk local time asymmetry observed by Lühr and Zhou (2020b) for Hp30 ≥ 3 is confirmed by the upper left graph in Figure 7. At these geomagnetic activity levels, the total near-Earth magnetospheric field is largest in the dusk sector with a maximum near 19:00 SMLT, and smallest in the dawn sector with a

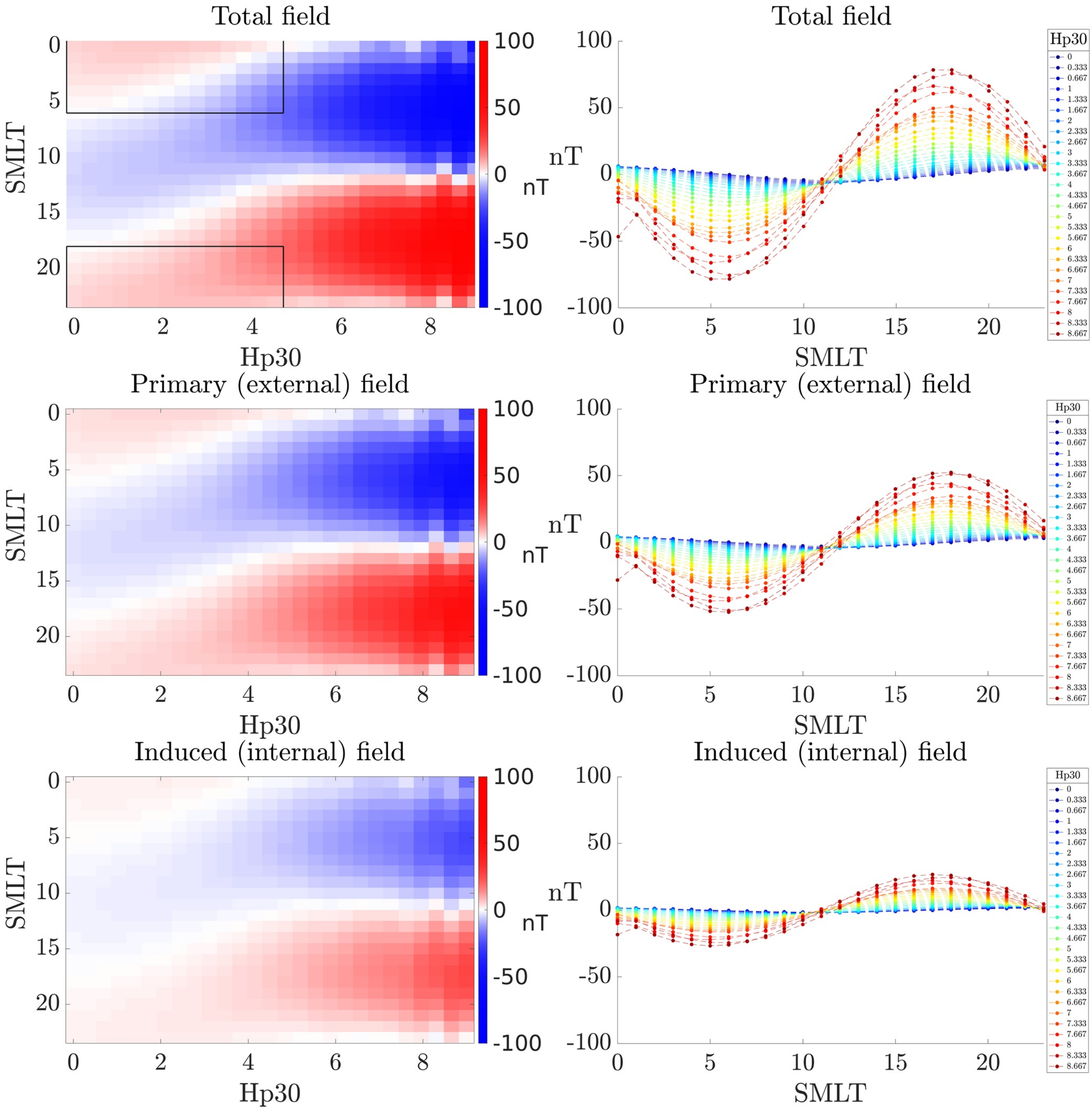

Figure 7. Average asymmetric part of the south component of the total (first row), primary (second row) and induced (third row) magnetospheric magnetic fields between 1 January 1997 and 31 December 2022 at the magnetic equator in CD coordinates predicted by the non-zonal terms of the degree 2 model (L2). Graphs in the left column show the average asymmetric part as a function of MLT and the Hp30 index. Graphs in the right column show profiles for selected Hp30 values of the field amplitude with MLT. The portion of the upper left panel delimited by black lines corresponds to the limits of Figure 4 of Lühr and Zhou (2020b).

minimum near 06:00 SMLT. Additionally, the upper right graph in Figure 7 shows that the amplitude of the local time asymmetry increases gradually with increasing geomagnetic activity, as was also observed by Lühr and Zhou (2020b). For Hp30 = 3, the maximum average asymmetry is roughly 10 nT, which is in good agreement with values in Figure 4 of Lühr and Zhou (2020b). For Hp30 = 8.7, it reaches about 60 nT. These observations support that our degree 2 model can recover local time asymmetries of the near-Earth magnetospheric field for both moderate and high geomagnetic activity levels. Several electric current systems were proposed to explain the dawn-dusk asymmetry, such as the partial ring current and the associated field-aligned currents (Le et al., 2011; Love & Gannon, 2010; Sitnov et al., 2017), or a dawnside wedge current system (Ohtani et al., 2018, 2021). We also note that magnetic signals generated by electric currents in the outer magnetosphere, such as the tail current system, could also contribute.

In Section 5, we showed that the degree 2 model was in better agreement with satellite data than CHAOS-7.15 for moderate and high geomagnetic activity levels. It appears from the discussion above that the local time asymmetry that grows at such activity levels is a key factor why the degree 2 model fits satellite data better than lower-degree models. However, an even higher degree model, L3, didn't improve the fit to the data, presumably due to contamination by un-modeled ionospheric fields. Our best model, L2, represents a compromise between the ability to represent fast-varying local-time asymmetries and the minimization of contamination by un-modeled ionospheric fields.

A local time asymmetry can also be observed for quiet geomagnetic activity levels, defined as $\mathrm{Hp30} \leq 2$ (see the upper left panel of Figure 7). Unlike the dawn-dusk asymmetry observed for moderate and active geomagnetic levels, this asymmetry peaks near 00:00 SMLT and is smallest near 12:00 SMLT. It also has a smaller amplitude, of no more than a few nT. From $\mathrm{Hp30} = 2$ to 4, the asymmetric part of the field smoothly transitions from a day-night to a dawn-dusk orientation. We attribute this day-night asymmetry of our model during geomagnetically quiet times to contamination by the ionospheric field for the following reasons. First, in Section 5, the fit of the degree 2 model to satellite data was shown to be slightly less good than the fit of the degree 1 model during quiet times, which we attributed to contamination by ionospheric fields. Second, the asymmetry is strongest during daytime and nighttime, as would be expected if caused by a primarily dayside ionospheric signal. The fact that no significant signal for quiet geomagnetic times is observed in Figure 4 of Lühr and Zhou (2020b), which was built from nighttime satellite data, further supports this interpretation.

As our model naturally separated primary and induced components of the magnetic field, it can be used to investigate the asymmetry in both components separately. The middle and bottom graphs in Figure 7 show the asymmetry for the primary and induced fields. These two fields have very similar variations as a function of SMLT and geomagnetic activity. This is expected and follows from the use of a one-dimensional conductivity model when separating primary and induced fields (cf. Section 3). Indeed, if one assumes that the conductivity of the Earth only varies radially, each external spherical harmonic of degree l and order m induces a field that can be exactly described by an internal spherical harmonic of the same degree l and order m (Olsen, 1999). We find that the induced field amplitude is about 30% of the total field amplitude. Note that the induced field is not constrained by the data, but is computed a posteriori assuming a 1D conductivity model–see Equations 10 and 11.

6.2. Geomagnetic Storms of 22 July 2009 and 29 May 2010

We now illustrate how the degree 2 model can be used to study individual geomagnetic storms, using the storms of 22 July 2009 and 29 May 2010 as examples. Details on the characteristics of these storms are provided in Le et al. (2011) and, for the most part, are not relevant to this study. These two storms are appropriate to evaluate the model since they were both associated with substantial variations of the near-Earth magnetospheric field with local time. These variations were studied by Le et al. (2011) using magnetic data from the C/NOFS satellite (de La Beaujardière, 2004). The C/NOFS satellite orbited on a low inclination orbit with a period of 97 min and an apogee and perigee of approximately 865 and 400 km, respectively. It is well suited to study the local time asymmetry of the near-earth magnetospheric field as it covers all local time sectors within one orbit. Figures 3 and 4 of Le et al. (2011) show the local time variations of the residuals between the North component of the field measured by the C/NOFS satellite and the IGRF-13 model (Alken et al., 2021) at different stages of the storms. We investigate if these variations can be reproduced by our model.

Figures 8 and 9 show the local time variations of the south component of the total field predicted by the degree 2 model (L2) at the magnetic equator in CD coordinates and at the Earth's surface, and for the storms of 22 July 2009 and 29 May 2010, respectively. These figures are designed to be easily compared with Figures 3 and 4 of Le et al. (2011). They show the same stages of each storm using the same format, introduced by Love and Gannon (2010). Note that the sign of the magnetic field is opposite to that in Figures 3 and 4 of Le et al. (2011), as they showed the North component instead of the south component. For each selected time, the center of the circle best fitting the model is shown as a red cross. When the predicted field is perfectly symmetric, the red cross is at

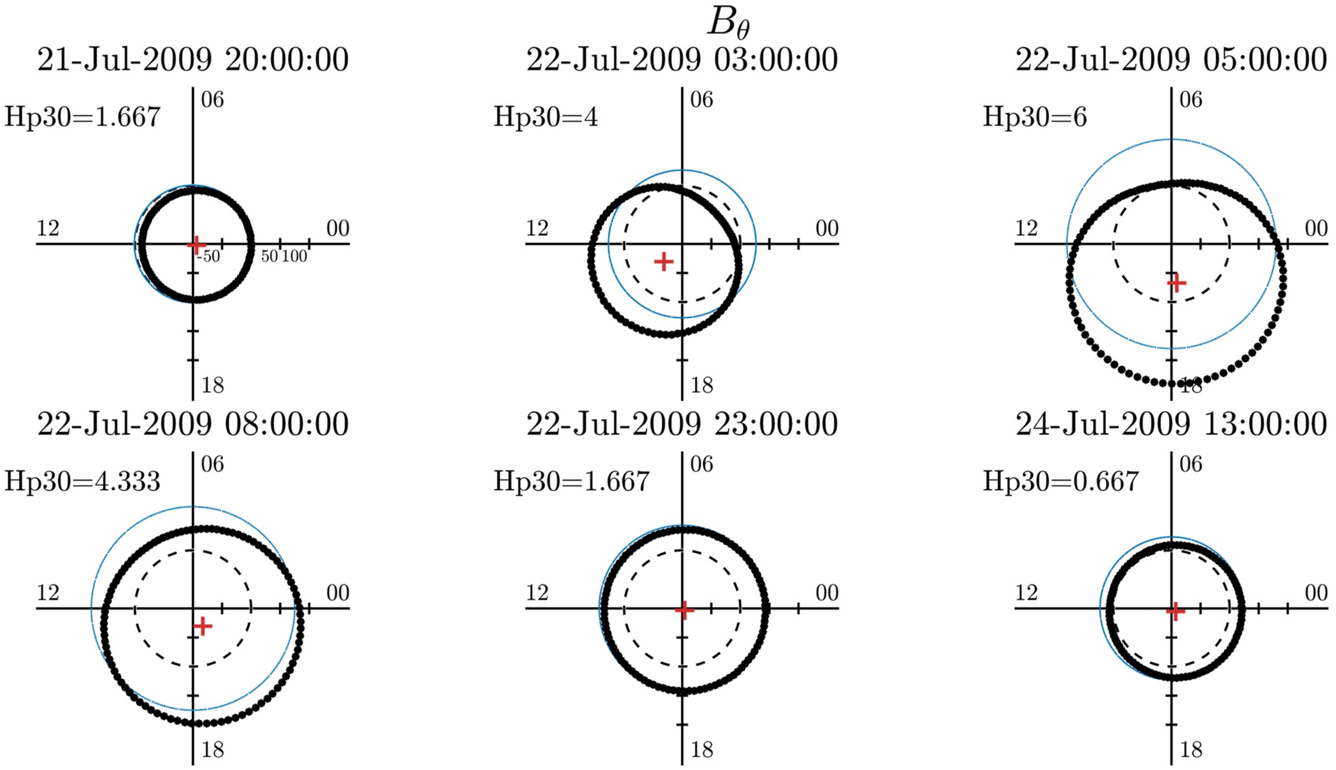

Figure 8. Local time variations of the south component of the field at the magnetic equator in CD coordinates predicted by the degree 2 model (L2) at several stages of the 22 July 2009 storm. In each graph, the local time is the angle from the horizontal axis measured counterclockwise. The magnitude of the magnetic field is proportional to the difference in radius from the dashed black circle, where the magnitude is set to 0 nT, and is shown by the labels below the positive *x*-axis. The degree 2 model prediction is shown with black dots. The blue circles indicate the value of minus the Dst index. The red crosses show the centers of the circle that best fits the model predictions.

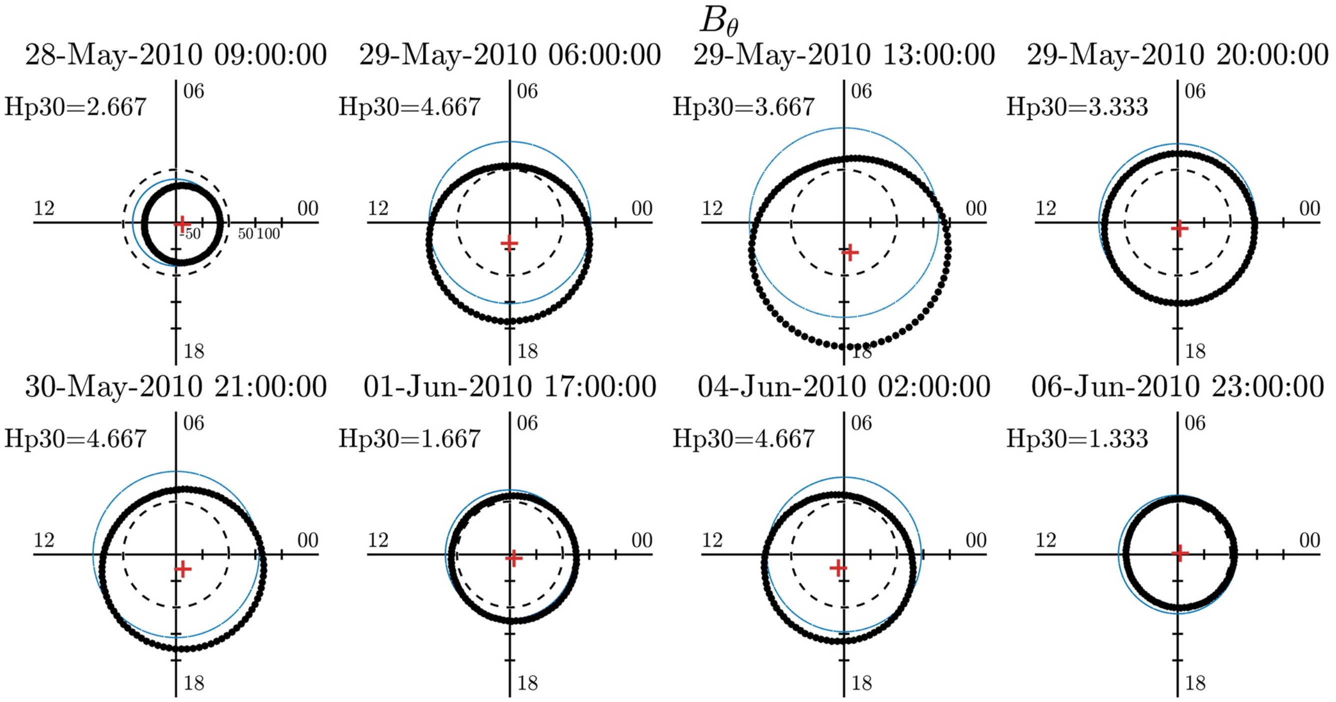

Figure 9. Same as Figure 8 but for the storm of 29 May 2010.

the origin. Any deviation of the red cross from the origin toward a certain local time indicates some asymmetry in the field. The larger the distance from the origin, the stronger the asymmetry.

The results presented in Figure 8 are in good qualitative agreement with those in Figure 3 of Le et al. (2011). In Figure 8, the main characteristics of the 22 July 2009 storm are reproduced. On 21 July 2009 at 20:00 UTC—upper left panel—which corresponds to the pre-storm period, the south component predicted by the model almost follows the Dst circle indicating that the field is mostly symmetric. This is confirmed by the center of the best-fitting circle, which is almost at the origin. On 22 July 2009 at 03:00 UTC 05:00 UTC and 08:00 UTC, corresponding to the main phase and the early recovery phase, some clear local time asymmetries can be observed, mostly oriented dawn-dusk. This is confirmed by the positions of the centers of the best-fitting circles, which are consistent with those in Figure 3 of Le et al. (2011). Note, however, that some differences can also be found. For example, on 22 July 2009 at 03:00 UTC, the asymmetry is dawn-dusk in Figure 3 of Le et al. (2011), whereas it is slightly tilted toward the dayside in Figure 8. A close inspection also shows some small magnitude differences between the magnetic fields in the two figures. As C/NOFS data were not corrected for the ionospheric field and the outer magnetospheric field, it is likely that these un-modeled fields contribute to these differences. Furthermore, as opposed to the model predictions in Figure 8, the satellite data are not synchronous, as it took 97 min for the C/NOFS satellite to complete a full orbit. Some significant time variations occur within 97 min during a geomagnetic storm, which could also contribute to the differences observed between the two figures.

The results in Figure 9 are also in good agreement with those in Figure 4 of Le et al. (2011). On 28 May 2020 at 09:00 UTC, a very small day-night asymmetry can be observed consistently with the corresponding panel in Figure 4 of Le et al. (2011). This is attributed to the compressed state of the magnetosphere during the initial phase of the magnetic storm (Le et al., 2011). On 29 May 2010 at 06:00 UTC and 13:00 UTC, the magnetic storm was in its main phase, and, as expected, a strong dawn-dusk asymmetry can be observed. Following the main phase, alternative episodes of storm recovery and ring current reactivation occur, as described by Le et al. (2011). The recovery episodes are illustrated by the panels on 29 May 2010 at 20:00 UTC, 1 June 2010 at 17:00 UTC and 6 June 2010 at 23:00 UTC, where the field is mostly symmetric. The ring current reactivation episodes, illustrated by the panels on 30 May 2010 at 21:00 UTC and 4 June 2010, on the other hand, show some larger dawn-dusk asymmetry, although not as large as during the main phase. This is again consistent with the results presented in Figure 4 of Le et al. (2011). The small differences between Figure 8 and the C/NOFS results are attributed to the same causes as above.

7. Conclusions

In this paper, we presented a new model of hourly variations of the near-Earth inner magnetospheric field and its induced counterpart spanning 25 years, from 1997 to 2022. The model was first validated by comparing the degree 1 and order 0, primary and induced spherical harmonic coefficients to the external and internal parts of the RC index. It was shown that the degree 1 and order 0 model coefficients and the RC index are consistent with one another to within a few nT. In particular, no significant quiet-time baseline shift was observed between these quantities.

The model was next compared to data from the Swarm, CHAMP and Ørsted satellites for the purpose of validation and performance assessment at LEO satellite altitude. This comparison was done independently for various geomagnetic activity levels characterized by the Hp30 index. The model performed best when the truncation degree was set to 2 for moderate and active geomagnetic activity levels, defined as Hp30 ≥ 2. At these geomagnetic activity levels, the fit of the degree 2 model to Swarm data was improved by up to 20% on all three components compared to the degree 1 model. The fit of the degree 2 model to Swarm data was also improved compared to the CHAOS-7.15 model on the south and east components for Hp30 ≥ 2, and on the radial component for Hp30 ≥ 4. The comparisons with CHAMP and Ørsted data mostly confirmed the results obtained with Swarm. However, there were some differences, which we attributed to less good local time coverage, and increased effects of ionospheric field contamination in the model at higher altitudes (in the case of Ørsted). For all satellites, a degree 3 model didn't improve the fit to the data.

An interesting feature of the new model is its ability to represent local time asymmetries. The model shows that, on average over 25 years, there is a significant dawn-dusk asymmetry for moderate and high geomagnetic activity levels. At moderate activity levels, this asymmetry is consistent with the dawn-dusk asymmetry observed by Lühr and Zhou (2020b) in residuals between CHAMP data and the CHAOS-6 model. The amplitude of the asymmetry increases gradually with geomagnetic activity. At high geomagnetic activity levels, it represents several tens of nT on average. The model is also able to independently reproduce results obtained with data from the C/NOFS satellite for the 22 July 2009 and 29 May 2010 geomagnetic storms (Le et al., 2011). Strong local time asymmetries of the order of 50 nT are observed during these two storms, which are attributed to field-aligned currents. While C/NOFS operated for only 7.5 years, our model is valid over 25 years, providing opportunities to investigate local-time asymmetries in the near-Earth magnetospheric field during many more geomagnetic storms. The new model also has the advantage of properly separating the primary and induced magnetic field, thus providing more accurate estimates of the magnitude of the external field generated by electric currents in the inner magnetosphere.

The process of developing this new model also provided insight into how un-modeled ionospheric magnetic fields can contaminate spherical harmonic models of the near-Earth magnetospheric field. Correcting ionospheric fields using a climatological model is a necessary but insufficient step, even during geomagnetic quiet times. The separation of magnetic signals generated in the inner and outer magnetosphere could also only be partially achieved, and some outer magnetospheric signals are likely captured by the model. These remain some important challenges for geomagnetic field modeling. In the future, new approaches will have to be developed to improve the separation between ionospheric and magnetospheric magnetic fields.

Data Availability Statement

A MATLAB software to compute the external and internal magnetic fields using the hourly time series of coefficients is available from martinfillionCIRES (2023). The weights W_l^n in Equations 12–14 are available at Zenodo via Kruglyakov and Kuvshinov (2023) under CC BY 4.0. The hourly observatory data used in this study were prepared by the British Geological Survey and can be retrieved from ftp://ftp.nerc-murchison.ac.uk/geomag/Swarm/AUX_OBS. The Swarm satellite data are available from http://swarm-diss.eo.esa.int/. The CHAMP data can be downloaded from http://isdc.gfz-potsdam.de and the Ørsted data can be downloaded from ftp://ftp.spacecenter.dk/data/magnetic-satellites. The internal and external parts of the RC index, as well as the CHAOS-7.15 model, can be retrieved from http://www.spacecenter.dk/files/magnetic-models/CHAOS-7/. The Dst index can be download from https://wdc.kugi.kyoto-u.ac.jp/dstdir/ and the Dcx index from http://dcx.oulu.fi/.

Acknowledgments
This research was supported by NASA Grant 80NSSC18K0468 and by NOAA cooperative agreements NA17OAR4320101 and NA22OAR4320151. AK has been partially supported in the framework of Swarm DISC activities, funded by ESA contract no. 4000109587, with support from EO Science for Society. MK was supported by the New Zealand Ministry of Business, Innovation and Employment through Endeavour Fund Research Programme contract UOOX2002. The results presented in this paper rely on data collected at magnetic observatories. We thank the national institutes that support them and INTERMAGNET for promoting high standards of magnetic observatory practice (https://www.intermagnet.org). We also thank the British Geological Survey and the World Data Center for Geomagnetism (Edinburgh) for making pre-processed and quality-controlled observatory data available. The European Space Agency (ESA) is gratefully acknowledged for providing processed and calibrated Swarm data. The authors also thank the German Aerospace Center (DLR) for the support to the CHAMP mission, and the Danish Government, NASA, ESA, CNES, DARA, and the Thomas B. Thriges Foundation for their support to the Ørsted mission.

References

Akasofu, S. I., & Chapman, S. (1964). On the asymmetric development of magnetic storm fields in low and middle latitudes. *Planetary and Space Science*, *12*(6), 607–626. https://doi.org/10.1016/0032-0633(64)90008-X

Alexeev, I. I., Belenkaya, E. S., Kalegaev, V. V., Feldstein, Y. I., & Grafe, A. (1996). Magnetic storms and magnetotail currents. *Journal of Geophysical Research*, *101*(A4), 7737–7747. https://doi.org/10.1029/95JA03509

Alken, P., Thébault, E., Beggan, C. D., Amit, H., Aubert, J., Baerenzung, J., et al. (2021). International geomagnetic reference field: The thirteenth generation. *Earth Planets and Space*, *73*(1), 49. https://doi.org/10.1186/s40623-020-01288-x

Balasis, G., Papadimitriou, C., & Boutsi, A. Z. (2019). Ionospheric response to solar and interplanetary disturbances: A swarm perspective. *Philosophical Transactions of the Royal Society A: Mathematical, Physical & Engineering Sciences*, *377*(2148), 20180098. https://doi.org/10.1098/rsta.2018.0098

Burke, W. J., Wilson, G. R., Lin, C. S., Rich, F. J., Wise, J. O., & Hagan, M. P. (2011). Estimating Dst indices and exospheric temperatures from equatorial magnetic fields measured by DMSP satellites. *Journal of Geophysical Research*, *116*(A1), A01205. https://doi.org/10.1029/2010JA015310

Califf, S., Alken, P., Chulliat, A., Anderson, B., Rock, K., Vines, S., et al. (2022). Investigation of geomagnetic reference models based on the Iridium$$ˆ{\circledR }$$constellation. *Earth Planets and Space*, *74*(1), 37. https://doi.org/10.1186/s40623-022-01574-w

Chulliat, A., Vigneron, P., & Hulot, G. (2016). First results from the swarm dedicated ionospheric field inversion chain. *Earth Planets and Space*, *68*(1), 104. https://doi.org/10.1186/s40623-016-0481-6

Chulliat, A., Vigneron, P., Thébault, E., Sirol, O., & Hulot, G. (2013). Swarm SCARF dedicated ionospheric field inversion chain. *Earth Planets and Space*, *65*(11), 1271–1283. https://doi.org/10.5047/eps.2013.08.006

deLa Beaujardière, O. (2004). C/NOFS: A mission to forecast scintillations. *Journal of Atmospheric and Solar-Terrestrial Physics*, *66*(17), 1573–1591. https://doi.org/10.1016/j.jastp.2004.07.030

Fillion, M., Hulot, G., Alken, P., & Chulliat, A. (2023). Modeling the climatology of low- and mid-latitude f-region ionospheric currents using the swarm constellation. *Journal of Geophysical Research: Space Physics*, *128*(5), e2023JA031344. https://doi.org/10.1029/2023JA031344

Finlay, C. C., Kloss, C., Olsen, N., Hammer, M. D., Tøffner-Clausen, L., Grayver, A., & Kuvshinov, A. (2020). The CHAOS-7 geomagnetic field model and observed changes in the South Atlantic Anomaly. *Earth Planets and Space*, *72*(1), 156. https://doi.org/10.1186/s40623-020-01252-9

Finlay, C. C., Lesur, V., Thébault, E., Vervelidou, F., Morschhauser, A., & Shore, R. (2017). Challenges handling magnetospheric and ionospheric signals in internal geomagnetic field modelling. *Space Science Reviews*, *206*(1–4), 157–189. https://doi.org/10.1007/s11214-016-0285-9

Finlay, C. C., Olsen, N., Kotsiaros, S., Gillet, N., & Tøffner-Clausen, L. (2016). Recent geomagnetic secular variation from Swarm and ground observatories as estimated in the CHAOS-6 geomagnetic field model. *Earth Planets and Space*, *68*(1), 112. https://doi.org/10.1186/s40623-016-0486-1

Friis-Christensen, E., Lühr, H., & Hulot, G. (2006). Swarm: A constellation to study the Earth's magnetic field. *Earth Planets and Space*, *58*(4), 351–358. https://doi.org/10.1186/BF03351933

Ganushkina, N. Y., Liemohn, M. W., & Dubyagin, S. (2018). Current systems in the Earth's magnetosphere. *Reviews of Geophysics*, *56*(2), 309–332. https://doi.org/10.1002/2017RG000590

Grayver, A. V., Kuvshinov, A., & Werthmüller, D. (2021). Time-domain modeling of three-dimensional Earth's and planetary electromagnetic induction effect in ground and satellite observations. *Journal of Geophysical Research: Space Physics*, *126*(3), e2020JA028672. https://doi.org/10.1029/2020JA028672

Haaland, S., & Gjerloev, J. (2013). On the relation between asymmetries in the ring current and magnetopause current. *Journal of Geophysical Research: Space Physics*, *118*(12), 7593–7604. https://doi.org/10.1002/2013JA019345

Hamilton, B. (2013). Rapid modelling of the large-scale magnetospheric field from Swarm satellite data. *Earth Planets and Space*, *65*(11), 10–1308. https://doi.org/10.5047/eps.2013.09.003

Hulot, G., Sabaka, T., Olsen, N., & Fournier, A. (2015). The present and future geomagnetic field. *Treatise on Geophysics*, 33–78. https://doi.org/10.1016/B978-0-444-53802-4.00096-8

Iyemori, T., Takeda, M., Nose, M., Odagi, Y., & Toh, H. (2010). Mid-latitude geomagnetic indices ASY and SYM for 2009 (Provisional). In *Internal report of data analysis center for geomagnetism and space magnetism*. Kyoto University.

Karinen, A., & Mursula, K. (2006). Correcting the Dst index: Consequences for absolute level and correlations. *Journal of Geophysical Research*, *111*(A8), A08207. https://doi.org/10.1029/2005JA011299

Kruglyakov, M., & Kuvshinov, A. (2023). *Weights to calculate induced part of magnetic scalar potential in time domain for radially-symmetric conductivity model of the earth*. Zenodo. https://doi.org/10.5281/zenodo.8054840

Kruglyakov, M., Kuvshinov, A., & Nair, M. (2022). A proper use of the adjacent land-based observatory magnetic field data to account for the geomagnetic disturbances during offshore directional drilling. *Space Weather*, *20*(12), e2022SW003238. https://doi.org/10.1029/2022SW003238

Kuvshinov, A., Grayver, A., Tøffner-Clausen, L., & Olsen, N. (2021). Probing 3-D electrical conductivity of the mantle using 6 years of Swarm, CryoSat-2 and observatory magnetic data and exploiting matrix Q-responses approach. *Earth Planets and Space*, *73*(1), 67. https://doi.org/10.1186/s40623-020-01341-9

Kuvshinov, A. V. (2008). 3-D global induction in the oceans and solid earth: Recent progress in modeling magnetic and electric fields from sources of magnetospheric, ionospheric and oceanic origin. *Surveys in Geophysics*, *29*(2), 139–186. https://doi.org/10.1007/s10712-008-9045-z

Langel, R., Sabaka, T., Baldwin, R., & Conrad, J. (1996). The near-Earth magnetic field from magnetospheric and quiet-day ionospheric sources and how it is modeled. *Physics of the Earth and Planetary Interiors*, *98*(3–4), 235–267. https://doi.org/10.1016/S0031-9201(96)03190-1

Laundal, K. M., & Richmond, A. D. (2017). Magnetic coordinate systems. *Space Science Reviews*, *206*(1–4), 27–59. https://doi.org/10.1007/s11214-016-0275-y

Le, G., Burke, W. J., Pfaff, R. F., Freudenreich, H., Maus, S., & Lühr, H. (2011). C/NOFS measurements of magnetic perturbations in the low-latitude ionosphere during magnetic storms. *Journal of Geophysical Research*, *116*(A12), A12230. https://doi.org/10.1029/2011JA017026

Lesur, V., Wardinski, I., Hamoudi, M., & Rother, M. (2010). The second generation of the GFZ reference internal magnetic model: GRIMM-2. *Earth Planets and Space*, *62*(10), 6–773. https://doi.org/10.5047/eps.2010.07.007

Lesur, V., Wardinski, I., Rother, M., & Mandea, M. (2008). GRIMM: The GFZ reference internal magnetic model based on vector satellite and observatory data. *Geophysical Journal International*, *173*(2), 382–394. https://doi.org/10.1111/j.1365-246X.2008.03724.x

Lesur, V., Whaler, K., & Wardinski, I. (2015). Are geomagnetic data consistent with stably stratified flow at the core–mantle boundary? *Geophysical Journal International*, *201*(2), 929–946. https://doi.org/10.1093/gji/ggv031

Love, J. J., & Gannon, J. L. (2009). Revised D_{st} and the epicycles of magnetic disturbance 1958–2007. *Annales Geophysicae*, *27*(8), 3101–3131. https://doi.org/10.5194/angeo-27-3101-2009

Love, J. J., & Gannon, J. L. (2010). Movie-maps of low-latitude magnetic storm disturbance. *Space Weather*, *8*(6), S06001. https://doi.org/10.1029/2009SW000518

Love, J. J., Rigler, E. J., Pulkkinen, A., & Riley, P. (2015). On the lognormality of historical magnetic storm intensity statistics: Implications for extreme-event probabilities. *Geophysical Research Letters*, *42*(16), 6544–6553. https://doi.org/10.1002/2015GL064842

Lühr, H., & Maus, S. (2010). Solar cycle dependence of quiet-time magnetospheric currents and a model of their near-Earth magnetic fields. *Earth Planets and Space*, *62*(10), 843–848. https://doi.org/10.5047/eps.2010.07.012

Lühr, H., Xiong, C., Olsen, N., & Le, G. (2017). Near-Earth magnetic field effects of large-scale magnetospheric currents. *Space Science Reviews*, *206*(1–4), 521–545. https://doi.org/10.1007/s11214-016-0267-y

Lühr, H., & Zhou, Y. (2020b). Residuals to the CHAOS-6 geomagnetic field model caused by magnetospheric currents during enhanced magnetic activity. *Geochemistry, Geophysics, Geosystems*, *21*(6), e2020GC008976. https://doi.org/10.1029/2020GC008976

Lühr, H., & Zhou, Y.-L. (2020a). Relation between the asymmetric ring current effect and the anti-sunward auroral currents, as deduced from CHAMP observations. *Annales Geophysicae*, *38*(3), 749–764. https://doi.org/10.5194/angeo-38-749-2020

Macmillan, S., & Olsen, N. (2013). Observatory data and the Swarm mission. *Earth Planets and Space*, *65*(11), 1355–1362. https://doi.org/10.5047/eps.2013.07.011

martinfillionCIRES (2023). CIRES-geomagnetism/model-of-the-near-Earth- magnetospheric-field-from-the-inner-magnetosphere: Initial release. https://doi.org/10.5281/zenodo.8429047

Matzka, J., Stolle, C., Yamazaki, Y., Bronkalla, O., & Morschhauser, A. (2021). The geomagnetic *Kp* index and derived indices of geomagnetic activity. *Space Weather*, *19*(5), e2020SW002641. https://doi.org/10.1029/2020SW002641

Maus, S., & Lühr, H. (2005). Signature of the quiet-time magnetospheric magnetic field and its electromagnetic induction in the rotating Earth. *Geophysical Journal International*, *162*(3), 755–763. https://doi.org/10.1111/j.1365-246X.2005.02691.x

Maus, S., Lühr, H., Balasis, G., Rother, M., & Mandea, M. (2005). Introducing POMME, the POtsdam magnetic model of the Earth. In C. Reigber, H. Lühr, P. Schwintzer, & J. Wickert (Eds.), *Earth observation with CHAMP: Results from three years in orbit* (pp. 293–298). Springer. https://doi.org/10.1007/3-540-26800-6_46

Maus, S., Rother, M., Stolle, C., Mai, W., Choi, S., Lühr, H., et al. (2006). Third generation of the Potsdam magnetic model of the Earth (POMME): Potsdam magnetic model of the Earth. *Geochemistry, Geophysics, Geosystems*, *7*(7), Q07008. https://doi.org/10.1029/2006GC001269

Maus, S., & Weidelt, P. (2004). Separating the magnetospheric disturbance magnetic field into external and transient internal contributions using a 1D conductivity model of the Earth: Separating the disturbance magnetic field. *Geophysical Research Letters*, *31*(12), L12614. https://doi.org/10.1029/2004GL020232

Milan, S. E., Clausen, L. B. N., Coxon, J. C., Carter, J. A., Walach, M.-T., Laundal, K., et al. (2017). Overview of solar wind–magnetosphere–ionosphere–atmosphere coupling and the generation of magnetospheric currents. *Space Science Reviews*, *206*(1–4), 547–573. https://doi.org/10.1007/s11214-017-0333-0

Mursula, K., Holappa, L., & Karinen, A. (2008). Correct normalization of the Dst index. *Astrophysics and Space Sciences Transactions*, *4*(2), 41–45. https://doi.org/10.5194/astra-4-41-2008

Mursula, K., Holappa, L., & Karinen, A. (2011). Uneven weighting of stations in the Dst index. *Journal of Atmospheric and Solar-Terrestrial Physics*, *73*(2), 316–322. https://doi.org/10.1016/j.jastp.2010.04.007

Mursula, K., & Karinen, A. (2005). Explaining and correcting the excessive semiannual variation in the Dst index. *Geophysical Research Letters*, *32*(14), L14107. https://doi.org/10.1029/2005GL023132

Neubert, T., Mandea, M., Hulot, G., von Frese, R., Primdahl, F., Jørgensen, J. L., et al. (2001). Ørsted satellite captures high-precision geomagnetic field data. *Eos, Transactions American Geophysical Union*, *82*(7), 81–88. https://doi.org/10.1029/01EO00043

Newell, P. T., & Gjerloev, J. W. (2012). SuperMAG-based partial ring current indices. *Journal of Geophysical Research*, *117*(A5), A05215. https://doi.org/10.1029/2012JA017586

Ohtani, S. (2021). Revisiting the partial ring current model: Longitudinal asymmetry of ground magnetic depression during geomagnetic storms. *Journal of Geophysical Research: Space Physics*, *126*(9), e2021JA029643. https://doi.org/10.1029/2021JA029643

Ohtani, S., Gjerloev, J. W., Anderson, B. J., Kataoka, R., Troshichev, O., & Watari, S. (2018). Dawnside wedge current system formed during intense geomagnetic storms. *Journal of Geophysical Research: Space Physics*, *123*(11), 9093–9109. https://doi.org/10.1029/2018JA025678

Ohtani, S., Imajo, S., Nakamizo, A., & Gjerloev, J. W. (2021). Globally correlated ground magnetic disturbances during substorms. *Journal of Geophysical Research: Space Physics*, *126*(4), e2020JA028599. https://doi.org/10.1029/2020JA028599

Olsen, N. (1999). Induction studies with satellite data. *Surveys in Geophysics*, *20*(3), 309–340. https://doi.org/10.1023/A:1006611303582

Olsen, N., Friis-Christensen, E., Floberghagen, R., Alken, P., Beggan, C. D., Chulliat, A., et al. (2013). The swarm satellite constellation application and research facility (SCARF) and swarm data products. *Earth Planets and Space*, *65*(11), 1189–1200. https://doi.org/10.5047/eps.2013.07.001

Olsen, N., Glassmeier, K.-H., & Jia, X. (2010). Separation of the magnetic field into external and internal parts. *Space Science Reviews*, *152*(1–4), 135–157. https://doi.org/10.1007/s11214-009-9563-0

Olsen, N., Lühr, H., Finlay, C. C., Sabaka, T. J., Michaelis, I., Rauberg, J., & Tøffner-Clausen, L. (2014). The CHAOS-4 geomagnetic field model. *Geophysical Journal International*, *197*(2), 815–827. https://doi.org/10.1093/gji/ggu033

Olsen, N., Sabaka, T. J., & Lowes, F. (2005). New parameterization of external and induced fields in geomagnetic field modeling, and a candidate model for IGRF 2005. *Earth Planets and Space*, *57*(12), 1141–1149. https://doi.org/10.1186/BF03351897

Olsen, N., & Stolle, C. (2012). Satellite geomagnetism. *Annual Review of Earth and Planetary Sciences*, *40*(1), 441–465. https://doi.org/10.1146/annurev-earth-042711-105540

Papadimitriou, C., Balasis, G., Boutsi, A. Z., Antonopoulou, A., Moutsiana, G., Daglis, I. A., et al. (2021). Swarm-derived indices of geomagnetic activity. *Journal of Geophysical Research: Space Physics*, *126*(11), e2021JA029394. https://doi.org/10.1029/2021JA029394

Püthe, C., & Kuvshinov, A. (2014). Mapping 3-D mantle electrical conductivity from space: A new 3-D inversion scheme based on analysis of matrix Q-responses. *Geophysical Journal International*, *197*(2), 768–784. https://doi.org/10.1093/gji/ggu027

Reigber, C., Lühr, H., & Schwintzer, P. (2002). CHAMP mission status. *Advances in Space Research*, *30*(2), 129–134. https://doi.org/10.1016/S0273-1177(02)00276-4

Richmond, A. D. (1995). Ionospheric electrodynamics using magnetic apex coordinates. *Journal of Geomagnetism and Geoelectricity*, *47*(2), 191–212. https://doi.org/10.5636/jgg.47.191

Sabaka, T. J., Hulot, G., & Olsen, N. (2010). Mathematical properties relevant to geomagnetic field modeling. In W. Freeden, M. Zuhair Nashed, & T. Sonar (Eds.), *Handbook of geomathematics*. Springer. https://doi.org/10.1007/978-3-642-27793-1_17-2

Sabaka, T. J., & Olsen, N. (2006). Enhancing comprehensive inversions using the Swarm constellation. *Earth Planets and Space*, *58*(4), 371–395. https://doi.org/10.1186/BF03351935

Sabaka, T. J., Olsen, N., & Langel, R. A. (2002). A comprehensive model of the quiet-time, near-Earth magnetic field: Phase 3. *Geophysical Journal International*, *151*(1), 32–68. https://doi.org/10.1046/j.1365-246X.2002.01774.x

Sabaka, T. J., Olsen, N., & Purucker, M. E. (2004). Extending comprehensive models of the Earth's magnetic field with Ørsted and CHAMP data. *Geophysical Journal International*, *159*(2), 521–547. https://doi.org/10.1111/j.1365-246X.2004.02421.x

Sabaka, T. J., Olsen, N., Tyler, R. H., & Kuvshinov, A. (2015). CM5, a pre-Swarm comprehensive geomagnetic field model derived from over 12 yr of CHAMP, Ørsted, SAC-C and observatory data. *Geophysical Journal International*, *200*(3), 1596–1626. https://doi.org/10.1093/gji/ggu493

Sabaka, T. J., Tøffner-Clausen, L., Olsen, N., & Finlay, C. C. (2018). A comprehensive model of Earth's magnetic field determined from 4 years of Swarm satellite observations. *Earth Planets and Space*, *70*(1), 130. https://doi.org/10.1186/s40623-018-0896-3

Sabaka, T. J., Tøffner-Clausen, L., Olsen, N., & Finlay, C. C. (2020). CM6: A comprehensive geomagnetic field model derived from both CHAMP and swarm satellite observations. *Earth Planets and Space*, *72*(1), 80. https://doi.org/10.1186/s40623-020-01210-5

Sandhu, J. K., Rae, I. J., & Walach, M.-T. (2021). Challenging the use of ring current indices during geomagnetic storms. *Journal of Geophysical Research: Space Physics*, *126*(2), e2020JA028423. https://doi.org/10.1029/2020JA028423

Sitnov, M. I., Stephens, G. K., Tsyganenko, N. A., Ukhorskiy, A. Y., Wing, S., Korth, H., & Anderson, B. J. (2017). Spatial structure and asymmetries of magnetospheric currents inferred from high-resolution empirical geomagnetic field models. In *Dawn-dusk asymmetries in planetary plasma environments* (pp. 199–212). American Geophysical Union (AGU). https://doi.org/10.1002/9781119216346.ch15

Stolle, C., Michaelis, I., & Rauberg, J. (2016). The role of high-resolution geomagnetic field models for investigating ionospheric currents at low Earth orbit satellites. *Earth Planets and Space*, *68*(1), 110. https://doi.org/10.1186/s40623-016-0494-1

Stolle, C., Michaelis, I., Xiong, C., Rother, M., Usbeck, T., Yamazaki, Y., et al. (2021). Observing Earth's magnetic environment with the GRACE-FO mission. *Earth Planets and Space*, *73*(1), 51. https://doi.org/10.1186/s40623-021-01364-w

Sugiura, M. (1963). Hourly values of equatorial Dst for the IGY. Tech. Rep.

Thomson, A. W. P., & Lesur, V. (2007). An improved geomagnetic data selection algorithm for global geomagnetic field modelling. *Geophysical Journal International*, *169*(3), 951–963. https://doi.org/10.1111/j.1365-246X.2007.03354.x

Tsyganenko, N., Andreeva, V., Kubyshkina, M., Sitnov, M., & Stephens, G. (2021). Data-based modeling of the Earth's magnetic field. In *Magnetospheres in the solar system* (pp. 617–635). American Geophysical Union (AGU). https://doi.org/10.1002/9781119815624.ch39

Turner, N. E., Baker, D. N., Pulkkinen, T. I., & McPherron, R. L. (2000). Evaluation of the tail current contribution to Dst. *Journal of Geophysical Research*, *105*(A3), 5431–5439. https://doi.org/10.1029/1999JA000248

Winch, D. E., Ivers, D. J., Turner, J. P. R., & Stening, R. J. (2005). Geomagnetism and Schmidt quasi-normalization. *Geophysical Journal International*, *160*(2), 487–504. https://doi.org/10.1111/j.1365-246X.2004.02472.x

Xiong, C., & Lühr, H. (2014). An empirical model of the auroral oval derived from CHAMP field-aligned current signatures – Part 2. *Annales Geophysicae*, *32*(6), 623–631. https://doi.org/10.5194/angeo-32-623-2014

Yamazaki, Y., Matzka, J., Stolle, C., Kervalishvili, G., Rauberg, J., Bronkalla, O., et al. (2022). Geomagnetic activity index Hpo. *Geophysical Research Letters*, *49*(10), e2022GL098860. https://doi.org/10.1029/2022GL098860

Yamazaki, Y., & Maute, A. (2017). Sq and EEJ—A review on the daily variation of the geomagnetic field caused by ionospheric dynamo currents. *Space Science Reviews*, *206*(1–4), 299–405. https://doi.org/10.1007/s11214-016-0282-z

Yokoyama, N., & Kamide, Y. (1997). Statistical nature of geomagnetic storms. *Journal of Geophysical Research*, *102*(A7), 14215–14222. https://doi.org/10.1029/97JA00903